NASA/TP—20230013695

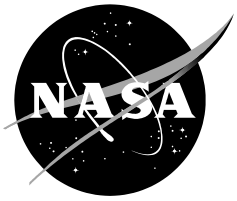

Assessing Flow Formability of Aerospace Aluminum Alloys via DIC Tensile Testing

Wesley A. Tayon
Langley Research Center, Hampton, Virginia

M. Cecilia Mulvaney
Langley Research Center, Hampton, Virginia

David E. Stegall
Langley Research Center, Hampton, Virginia

Jacob D. Hochhalter
University of Utah, Salt Lake City, Utah

December 2023

NASA STI Program Report Series

Since its founding, NASA has been dedicated to the advancement of aeronautics and space science. The NASA scientific and technical information (STI) program plays a key part in helping NASA maintain this important role.

The NASA STI program operates under the auspices of the Agency Chief Information Officer. It collects, organizes, provides for archiving, and disseminates NASA's STI. The NASA STI program provides access to the NTRS Registered and its public interface, the NASA Technical Reports Server, thus providing one of the largest collections of aeronautical and space science STI in the world. Results are published in both non-NASA channels and by NASA in the NASA STI Report Series, which includes the following report types:

- TECHNICAL PUBLICATION. Reports of completed research or a major significant phase of research that present the results of NASA Programs and include extensive data or theoretical analysis. Includes compilations of significant scientific and technical data and information deemed to be of continuing reference value. NASA counterpart of peer-reviewed formal professional papers but has less stringent limitations on manuscript length and extent of graphic presentations.

- TECHNICAL MEMORANDUM. Scientific and technical findings that are preliminary or of specialized interest, e.g., quick release reports, working papers, and bibliographies that contain minimal annotation. Does not contain extensive analysis.

- CONTRACTOR REPORT. Scientific and technical findings by NASA-sponsored contractors and grantees.

- CONFERENCE PUBLICATION. Collected papers from scientific and technical conferences, symposia, seminars, or other meetings sponsored or co-sponsored by NASA.

- SPECIAL PUBLICATION. Scientific, technical, or historical information from NASA programs, projects, and missions, often concerned with subjects having substantial public interest.

- TECHNICAL TRANSLATION. English-language translations of foreign scientific and technical material pertinent to NASA's mission.

Specialized services also include organizing and publishing research results, distributing specialized research announcements and feeds, providing information desk and personal search support, and enabling data exchange services.

For more information about the NASA STI program, see the following:

- Access the NASA STI program home page at http://www.sti.nasa.gov

- Help desk contact information:

https://www.sti.nasa.gov/sti-contact-form/
and select the "General" help request type.

NASA/TP—20230013695

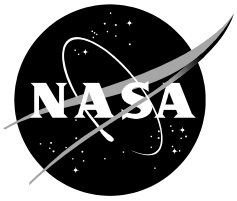

Assessing Flow Formability of Aerospace Aluminum Alloys via DIC Tensile Testing

Wesley A. Tayon
Langley Research Center, Hampton, Virginia

M. Cecilia Mulvaney
Langley Research Center, Hampton, Virginia

David E. Stegall
Langley Research Center, Hampton, Virginia

Jacob D. Hochhalter
University of Utah, Salt Lake City, Utah

National Aeronautics and
Space Administration

Langley Research Center
Hampton, VA 23681

December 2023

Abstract

Over the past decade, NASA Langley Research Center (LaRC) has championed integrally stiffened cylinder (ISC) technology for single-piece, cryogenic tank barrels on launch vehicles. The current investigation aims to extend the hybrid spin/shear/flow forming process to aircraft fuselage structures, a damage tolerance critical application. The WF Maschinenbau VUD-600® vertical spin/flow forming facility recently established at LaRC represents a reasonable sub-scale facsimile of the ISC deformation process for research and development (R&D) purposes.

The objective of this study is to explore whether tensile testing with digital image correlation (DIC) is an effective way to rank the formability of candidate aerospace Al alloys and expedite empirical forming trials. Specific tensile data, such as reduction of area, strain hardening exponent, and modulus of resilience, are used as formability metrics for a variety of alloy/temper/product form combinations. Results from high-strength aluminum alloys AA 2139, AA 2050, AA 2043 and AA 2219 are compared with the medium-strength, highly formable AA 6061 benchmark.

Rolled, forged and cast preform materials in both the -O temper (fully annealed) and -T4 temper (solution-treated, quenched, and naturally aged) conditions are evaluated. AA 2139 plate in the -T4 temper emerges as the top-ranked material, based on the criteria selected. Starting with preforms in the -T4 temper will result in flow-formed material exhibiting mechanical properties closer to aircraft fuselage requirements. The optimum balance between strength and damage tolerance may also be achieved via post-forming procedures that avoid quenching and stretching.

Table of Contents

Table of Figures

Table of Tables

Symbols and Abbreviations

A..... axial (orientation)
AA ..... Aluminum Association
Ag..... silver
Al..... aluminum
AR..... tensile reduction in area
ASTM ..... American Society for Testing and Materials
B..... billet (cast product)
C ..... circumferential (orientation)
Cr ..... chromium
Cu ..... copper
$\Delta\boldsymbol{\sigma}_{\boldsymbol{form}}$ ..... forming stress range
DIC..... digital image correlation
E..... elastic modulus
e ..... engineering strain
$\boldsymbol{e_t}$ ..... total tensile elongation
$\boldsymbol{e_u}$ ..... uniform tensile elongation
$\boldsymbol{e_{ys}}$ ..... engineer strain at 0.2% offset yield stress
$\boldsymbol{\varepsilon}$ ..... true strain
$\boldsymbol{\varepsilon_t}$..... true strain (thickness)
$\boldsymbol{\varepsilon_w}$..... true strain (width)
EDM ..... electrical discharge machining
ESA ..……European Space Agency
F ..... forging (rolled-ring-forged product)
Fe..... iron
GB..... grain boundary
GP..... Guinier-Preston (zones)
ISC ..... integrally stiffened cylinder
K..... strength coefficient
ksi..... thousand pounds per square inch
L ..... longitudinal (orientation)
LaRC..... Langley Research Center
Li ..... lithium
m..... strain rate sensitivity coefficient
Mg ..... magnesium

Mn ..... manganese

$\boldsymbol{n}$ ..... strain hardening exponent

P ..... plate (rolled product)

PLC ..... Portevin–Le Châtelier (effect/behavior)

$\boldsymbol{r}$ ..... plastic strain (anisotropy) ratio

R&D ..... research and development

RT ..... room temperature

$\boldsymbol{\sigma}$ ..... engineering stress

$\boldsymbol{\sigma_{true}}$ ..... true stress

$\boldsymbol{\sigma_{ys}}$ ..... (engineering) 0.2% offset tensile yield strength

$\boldsymbol{\sigma_{uts}}$ ..... (engineering) ultimate tensile strength

SHT ..... solution heat treatment

Si ..... silicon

T ..... transverse (orientation)

Ti ..... titanium

TP ..... Technical Publication

$\boldsymbol{\mu_r}$ ..... modulus of resilience

$\boldsymbol{\mu_t}$ ..... modulus of toughness

V ..... vanadium

Zn ..... zinc

Zr ..... zirconium

1. Introduction

The major benefits for aerospace vehicles associated with the integrally stiffened cylinder (ISC) concept derive from the simplified manufacturing (lower part count) and improved reliability (fewer welds/joints) [1,2]. Adoption of the near-net-shape approach, led by NASA Langley Research Center (LaRC), has resulted in the successful production of cylindrical, thin-walled structures to close tolerances (Figure 1) [3]. Currently, integrally stiffened cylinder (ISC) fabrication begins with a thick-walled cylindrical preform produced by rolled ring forging (Figure 1a). The preform is flow formed over a mandrel that has recessed grooves on the exterior surface to produce the interior stiffener geometry on the workpiece (Figure 1b). Adjustable forming rollers provide the necessary force to flow the material along the axis of the cylinder, increasing the length of the part, while simultaneously thinning the wall. As the cylindrical shape forms, material is forced into the grooves to create longitudinal stiffeners on the inner surface. Fundamentally, the resultant triaxial plastic deformation consists of a location-dependent mix of rolling, extrusion, and forging strain components.

The ISC process has been successfully scaled-up to produce 10-ft-diameter barrel sections from a *medium-strength* Aluminum (Al) alloy, AA 6061 (Figure 1c). Further research is needed to guide process development for the *high-strength* Al alloys required in most aerospace applications. A vertical spin/flow forming machine was recently installed at LaRC as a research and development (R&D) facility supporting the maturation of ISC technology. The anatomy of the VUD-600, manufactured by WF Maschinenbau (Germany), is shown in Figure 2. The equipment configuration consists of two external forming rollers, a mandrel that defines the internal surface geometry of the formed part, and a tailstock which clamps the preform to the mandrel. The machine is designed to operate at temperatures close to ambient and can form parts up to 2 ft. in diameter and 3 ft. in length.

The basic operation of the VUD-600 involves the motion of a pair rollers relative to the workpiece attached to a rotating mandrel. The primary input variables include mandrel rotation speed, roller feed rate, roller angle, reduction per pass, roller offset, and the number of upward/downward passes. All the processing parameters necessary for each forming trial are programmed into the control system using G-code in two discrete stages. The first step involves spin forming from flat plate until mandrel contact, with minimal reduction in overall thickness. The second step involves flow forming along the mandrel to the target geometry, with substantial thickness reduction and axial elongation. Typically, a coolant/lubricant is continuously applied during forming operations to counteract adiabatic heating caused by the rapid deformation rate.

The VUD-600 represents a reasonable sub-scale facsimile of the ISC process. Mechanistically, ISC fabrication is a hybrid of the spin, shear and flow forming processes illustrated in Figure 3. Historically, these rotary modes have been employed to manufacture a multitude of axisymmetric products by fast, incremental deformation of a variety of preforms [4]. Common to all three methods, the plastic zone is confined to the contact area beneath the translating roller(s). Spin forming involves shape change with wall thickness remaining constant (Figure 3a), shear forming involves shape change with wall thickness reduction and possible change in diameter (Figure 3b), but flow forming causes a simultaneous reduction in wall thickness and an increase in length with the possibility for varying the diameter along the length (Figure 3c). The incremental deformation occurs at very high strain rate, and flow forming induces the most total strain through large reductions in thickness. In order to form a defect-free product, preform material must have sufficient compressive plasticity and tensile ductility to accommodate the complex, highly localized stress state generated [5].

Flow formability is not an intrinsic material property that can be quantified directly and depends on the relationship between material characteristics and processing conditions. Determination of flow forming capacity is critical because the mechanical response governs the probability of fabricating fully-formed, defect-free components. Flow forming technology has long been exploited in the automotive industry for axisymmetric (tubular) steel components, but more recently for Al alloy A356 wheels using cast preforms [6–8]. The European Space Agency (ESA) has utilized flow forming for production of steel solid rocket motor cases for the Ariane 5 launcher [2]. However, flow forming technology is not widely used within the aerospace industry, such that a universal, quantitative protocol for assessing flow-formability does not exist. Consequently, data covering either formability or forming parameters for high-performance Al alloys are sparse.

In general, formability (or workability) is a measure of the capacity of a metal to undergo plastic deformation to a given shape without cracking or tearing. Bulk workability can be conveniently described as a function of material characteristics (strength/ductility/plasticity) and deformation conditions (such as strain, strain rate, and temperature) [9, 10]. Duplicating the mix of compressive, tensile and shear stress components in a single flow formability test is impossible. Consequently, quantification frequently involves a compilation of data from various methods, including compression, tension, bending, and hardness tests [11]. Compression testing is usually employed to assess *bulk workability*, because the stress state and *level* of plastic strain are comparable. Tensile testing is commonly used to assess *sheet formability*, because the stress state and *type* of plastic strain are comparable. Although both techniques are compatible with assessment of flow-formability, tensile tests are attractive due to expedience and data reproducibility.

2. Materials and Test Methodology

2.1 Material Selection

ISC technology, developed for launch vehicles, is currently being explored for the fabrication of single-piece fuselage structures with different design allowable properties. *Dissimilar Al alloys in different temper conditions* is the norm for riveted skin-stringer fuselage construction on most aircraft. The incumbent skin material is AA 2024 in a damage tolerant temper (-T3), whereas the incumbent stringer material is AA 7075 in a high-strength temper (-T7). Applying ISC fabrication technology does pose unique challenges because most of the pressurized structure comprises material in *a single alloy/temper combination*. Flow-formed articles will likely be subjected to a post-forming heat treatment that achieves a suitable balance between damage tolerance and strength. Customarily, aerospace Al alloys are cold worked or formed in the -O temper because materials tend to be in the most ductile, lowest strength condition. Pertinent examples are AA 2024 and AA 7075 that both exhibit superior tube spinnability at room temperature (RT) when starting with preform material in the -O temper [12]. The concern is that thermal treatments that include rapid quenching from high temperature are subsequently required for tailoring mechanical properties to meet service specifications.

Solution heat treatment (SHT) of large, thin-walled, and complex-shaped articles always introduces the risk of quench distortion or loss of tolerance. Accordingly, flow forming of materials in alternate tempers may create the opportunity for post-forming heat treatment that *does not* include a rapid quenching step. A viable candidate is the -T4 temper that involves high-temperature SHT, followed by rapid quenching and natural (ambient temperature) aging to a ‘substantially stable’ condition. Sourcing preforms from bulk material in the -T4 temper will produce flow-formed articles with mechanical properties closer to the target. Adopting the approach will also introduce flexibility for effective heat treatment practices, such as direct artificial (intermediate temperature) aging. Thus, flow forming using preform material in the -T4 temper

can be advantageous to achieving balanced service properties in the final product, *but only provided that the formability is adequate*.

Along with alloy/temper combination, a comprehensive evaluation of the formability of candidate materials must include product form as a process variable. The preform for the full-scale ISC process is a thick-walled cylinder that can be a forged, extruded, or cast product. Rolled ring forgings were used for preform material, including alloys AA 6061, AA 2050, and AA 2219, for prior full-scale forming trials. In contrast, the common preform for the sub-scale VUD-600 forming trials is a circular flat plate, typically rolled product. The preforms for the VUD-600 have been sourced from plate products for alloys AA 6061, AA 2050, and AA 2139; and a cylindrical billet provided in the homogenized condition for alloy AA 2043. The suite of alloys and product forms included in this study are summarized below:

- Forging (full-scale): AA 6061, AA 2219, AA 2050
- Plate (sub-scale): AA 6061, AA 2139, AA 2050
- Billet (sub-scale): AA 2043

The different alloys and product forms will have different microstructures (grain size, texture, precipitates/particles) associated with the intrinsic differences in the processing methods and chemical compositions. Microstructures were not characterized in this study as the differences are inherent to each alloy and product form combination and are not something that the end-user can control, except with heat treatment/temper.

High stiffness, strength, and damage tolerance feature prominently in the design property allowables for both launch vehicle and aircraft structures. However, damage tolerance has a much higher priority for multiple-use than single-use applications, e.g., fatigue resistance. Thus, the flow-formed Al alloy candidates must be capable of service properties that represent a compromise between AA 2024-T3 and AA 7075-T7 materials. The focus is on high-solute 2xxx series alloys because good weldability is a bonus for assembling fuselages from ISC barrel sections. The nominal elemental compositions of the candidate Al alloys included in this study are listed in Table 1, and the reasons for selection are presented below:

- AA 2139 is an Al-Cu-Mg-Ag alloy that can achieve -T8 properties in the -T6 temper condition [13]. This attribute is beneficial to heat treatment of near-net shape parts, where introducing pre-aging cold work is very difficult. AA 2139 provides excellent damage tolerance and has seen application as a ballistic material for armored military vehicles [14].
- AA 2050 is a third generation Al-Li alloy with improved strength, fracture toughness, and fatigue crack growth resistance and reduced density compared to traditional aluminum alloys [15]. The alloy is produced in plate thicknesses up to 5 inches by reducing quench sensitivity issues associated with prior Al-Li alloys [16].
- AA 2043 is another third generation Al-Li alloy with high fracture toughness, and specifically improved short-transverse fracture toughness, along with good corrosion and fatigue resistance. This alloy has a Ag-free composition to control production costs and avoid patent infringement [17].
- AA 2219 is a weldable, high Cu alloy with good strength, fracture toughness, and corrosion resistance that has a long cryogenic tank pedigree, such as the Space Shuttle [18].

AA 6061 is not a candidate alloy for fuselage consideration due to the higher density and lower strength compared to the 2xxx series alloys. However, AA 6061 has demonstrated excellent formability at multiple scales during ISC process development. Therefore, AA 6061 serves as a benchmark for all 2xxx series to be compared against.

Traditionally, ISC fabrication has been executed on Al alloys in the fully-annealed (-O temper) condition to maximize the probability of complete barrel formation. In order to achieve the -O temper condition, annealing treatments were conducted in accordance with AMS 2770 [19] as

follows: heat to 775°F, hold parts at 775°F for one-hour, controlled furnace cool down to 500°F at a maximum rate of 50°F per hour, remove part from furnace and allow air cooling to room temperature (RT). To achieve the -T4 temper condition, the SHT temperature is governed by the phase diagram and specific alloy chemistry. The temperatures used for each alloy included in this study are shown in Table 2. Individual alloys were exposed to the appropriate temperature for 1 hour, immediately water quenched, and naturally aged for a minimum of 3 days to achieve the -T4 temper condition. AA 6061 and AA 2043 were heat treated at LaRC to a -T4 temper as part of this study. AA 2050 and AA 2139 were received in a -T4 temper, so no heat treatment was necessary. Recognizing that AA 2219 exhibits poor RT ISC formability in the -O temper condition as documented from a prior full-scale forming campaign [20], material in the -T4 temper was not considered for formability testing.

2.2 Testing Methods

Practitioners of rotary forming employ a battery of formability metrics, the choice depending on the type of process and gage of material (sheet vs. bulk). Tensile testing methods and metrics gleaned from sheet metal formability studies [21–24], plus previous knowledge from flow formability assessments [20, 25] are applicable. Sheet formability studies suggest that uniform elongation ($\boldsymbol{\varepsilon_u}$), strain rate sensitivity coefficient (***m***), strain hardening exponent (***n***), and plastic strain or anisotropy ratio (***r***) are key material characteristics. Similarly, prior assessments of flow formability via tensile testing indicate that ***n***, reduction in area (***AR***), and modulus of resilience ($\boldsymbol{\mu_r}$) may be the key parameters [25]. Additionally, ***AR***, ***n***, and total elongation ($\boldsymbol{e_t}$) are reported as indicators of spin formability [26].

All the metrics previously established are taken into consideration for assessing flow forming capacity of the materials included in this study. The main objective is to explore whether tensile testing combined with digital image correlation (DIC) is a viable screening method for assessing the flow formability of aerospace Al alloys. The immediate goal is to establish which of the various data generated by DIC tensile testing are best suited for ranking the formability of alloy/temper/product combinations. It is anticipated that the degree of plastic anisotropy (***r*** ratio), as determined by DIC, may play be pivotal in complex shape formation, e.g., stiffeners. The goal is to import select data into DEFORM® simulation software to provide sub-scale (VUD-600) forming parameters for aerospace Al alloys that convey to full-scale (ISC) fabrication [27].

The DIC technique is an optical method that is increasingly being employed to supplement the (average) strain data generated by extensometers or fiducial marks during tensile testing. Typical DIC data are excised from an image series of stochastically patterned surfaces during elasto-plastic deformation of metallic materials. Use of the precise, non-contact method for quantifying strain distribution and plastic anisotropy (***r***) has been adopted commercially to optimize sheet metal forming operations. Standard DIC protocols were employed to measure surface displacements and compute strains within the gage section. Two 5-megapixel cameras captured images at a frequency of 1 Hz with a 40 ms exposure time. The tensile test setup, an example of a specimen speckle pattern, and post-processed DIC strain data are shown in Figure 4. The surface from electrical discharge machining (EDM) proved to be more compatible with paint adhesion for DIC patterning than a milled surface.

Sub-size specimens were cut via wire EDM to dimensions in accordance with ASTM E8 [28] from the various alloy and product forms referenced previously. Tensile data for the axial (A) direction of the cylindrical preform (applies to billet and forging) material are compared with the longitudinal (L) orientation of the plate material. Similarly, data from the circumferential (C) orientation in the cylindrical preform (applies to billet and forging) are compared with data from the transverse (T) orientation in rolled plate product. Aluminum alloys exhibit very low strain rate sensitivity at room temperature [24, 25]. Therefore, tensile testing was conducted at a single

stroke rate of 0.02 in./min. on a screw-driven test rig. Average properties were computed from the results of two test specimens per orientation and heat treatment combination. Tensile testing generated engineering mechanical properties including ultimate tensile strength ($\boldsymbol{\sigma_{uts}}$), 0.2% offset tensile yield strength ($\boldsymbol{\sigma_{ys}}$), forming stress range ($\Delta\boldsymbol{\sigma_{form}} = \boldsymbol{\sigma_{uts}} - \boldsymbol{\sigma_{ys}}$), $\boldsymbol{e_t}$, $\boldsymbol{e_u}$, ***AR***, ***n***, ***r***, $\boldsymbol{\mu_r}$, and modulus of toughness ($\boldsymbol{\mu_t}$).

The strain hardening exponent was calculated using the Hollomon equation (Eq. 1), where $\boldsymbol{\sigma_{true}}$ is the true stress, ε is the true strain, ***n*** is the strain hardening exponent, and ***K*** is the strength coefficient. Hollomon's equation is a simple power-law fit to the true stress-strain curve in the plastic region, as described in ASTM E646 [29].

$$\sigma_{true} = K \cdot \varepsilon^n \qquad \text{(Eq. 1)}$$

The modulus of resilience ($\boldsymbol{\mu_r}$) represents the strain energy absorption prior to widespread plastic deformation and is the area under the elastic portion of the stress-strain curve, which is approximated as the area of a triangular-shaped region. It is defined by Eq. 2, where σ is the true stress, **ε** is the true strain, and ***E*** is the elastic modulus. In principle, the stress and strain at the proportional limit should be used in Eq. 2. However, with the subjectivity associated with determining the proportional limit, the stress and strain at the $\boldsymbol{\sigma_{ys}}$ can be used to approximate this value.

$$\mu_r \cong \int_0^{e_{ys}} \sigma \cdot de \cong \frac{\sigma_{ys} \cdot e_{ys}}{2} \cong \frac{\sigma_{ys}^2}{2E} \qquad \text{(Eq. 2)}$$

The modulus of toughness (μ_t) represents the strain energy absorption up to tensile failure computed as the integral of the area under the entire stress-strain curve in Eq. 3.

$$\mu_t = \int_0^{e_t} \sigma \cdot de \qquad \text{(Eq. 3)}$$

However, numerically this can be difficult to integrate with stress-strain data. As a result, an approximation for the full stress-strain curve is introduced in Eq. 4, where $\boldsymbol{\sigma_{uts}}$ is the ultimate tensile strength, $\boldsymbol{e_t}$ is the total elongation. This equation approximates the elastic region as a triangular area as in Eq. 3, and the plastic region as a rectangle with the height equal to the average of $\boldsymbol{\sigma_{ys}}$ and $\boldsymbol{\sigma_{uts}}$ and the length equal to plastic strain (the difference between $\boldsymbol{e_t}$ and $\boldsymbol{e_{ys}}$).

$$\mu_t \cong \mu_r + \left(\frac{\sigma_{ys}+\sigma_{uts}}{2}\right)\left(e_t - e_{ys}\right) = \frac{\sigma_{ys}^2}{2E} + \left(\frac{\sigma_{ys}+\sigma_{uts}}{2}\right)\left(e_t - \frac{\sigma_{ys}}{E}\right) \qquad \text{(Eq. 4)}$$

The plastic strain ratio (***r***) is defined in Eq. 5 as the ratio of the width strain to thickness strain, where ε_w is the true strain (width) and ε_t is the true strain (thickness).

$$r = \frac{\varepsilon_w}{\varepsilon_t} \qquad \text{(Eq. 5)}$$

ASTM E517 provides guidance on testing and analysis methods to determine the value of ***r*** in metallic materials [30]. The through-thickness strain is customarily computed by assuming constant volume during deformation, rather than measured directly. The ***r*** value is a metric of formability isotropy [31,32]. Essentially, the more isotropic the material plasticity, the closer the ***r*** value is to 1. Large departures from unity indicate increasing levels of anisotropy, a greater propensity for directional strain localization, and usually translate into reduced formability. Preferential thinning in the thickness direction of the test specimen produces ***r*** values < 1. In contrast, preferential thinning in the width direction of the test specimen is indicated by ***r*** values > 1. In this report, the thickness direction of the tensile specimen is the radial direction

for cylindrical preforms and the short-transverse direction for plate products. Note that ***r*** value is computed as function of strain (rather than assumed constant) because of the variability frequently encountered with high plastic strains [33].

3. Results

The tension test results for formability assessment are presented in multiple tables/figures below for specimens that were extracted from plate or cylindrical (forging and billet) preforms. The sub-sections that follow address specific properties for each alloy in both the -O and -T4 temper. Tensile properties for alloys in the -O temper are shown for the L orientation in Table 3 and for the T orientation in Table 4. Tensile properties for alloys in the -T4 temper are shown for the L orientation in Table 5 and for the T orientation in Table 6. The data for each alloy represent the average of two specimens per orientation and temper. Tensile $\boldsymbol{\sigma_{ys}}$, $\boldsymbol{\sigma_{uts}}$, $\Delta\boldsymbol{\sigma_{form}}$, $\boldsymbol{n}$, $\boldsymbol{\mu_r}$, and $\boldsymbol{\mu_t}$ had very low variability (generally less than 3%) between the two specimens. Greater variability within $\boldsymbol{e_u}$, $\boldsymbol{e_t}$, ***AR***, and ***r*** was observed simply due to the sensitivity of these parameters to plastic instabilities during necking. The parenthetical notations P, F, and B correspond to the product form of the preform material, i.e., plate, forging, and billet. In instances where the test data were similar for both material orientations, only the L/A data are discussed.

3.1 -O Temper Condition

The -O temper is recognized as the softest condition and generally provides the best formability based on previous flow forming studies [9]. A representative engineering stress-strain plot for each alloy in the -O temper condition is provided in Figure 5. The curves reveal that AA 6061 is the weakest of the alloys evaluated and that the 2xxx series alloys all exhibit higher strength, particularly AA 2139 and AA 2050. AA 6061 and AA 2139 show significantly greater ductility when compared to AA 2050, AA 2043 and AA 2219. AA 2050 and AA 6061 were examined in both plate and rolled ring forging product forms. Consistently, plate for each alloy offers greater elongation and ultimate strength than forged product.

A noticeable feature of the stress-strain curves is the serrated stress-strain response beyond the yield point, a phenomenon known as the Portevin–Le Châtelier (PLC) effect. The jerky plastic flow in Al alloys is a result of inhomogeneous deformation and has been associated with discontinuous dislocation motion [34]. AA 6061 exhibited subtle signs of PLC behavior, whereas the effect was readily observable between yield and the onset of necking in the 2xxx series alloys. These alloys tend to contain much more solute than AA 6061, a material attribute that magnifies the serration amplitude [35]. The lower formability of alloy/temper/product combinations that exhibit PLC behavior has been correlated with plastic flow localization leading to premature failure [34].

3.1.1 Tensile Strength

In the -O temper, AA 6061 had the lowest strength of all alloys tested with a $\boldsymbol{\sigma_{ys}}$ of 8 ksi to 9 ksi for both plate and forging, roughly half that of AA 2139, AA 2050, and AA 2219 (14 ksi to 19 ksi). AA 2043 $\boldsymbol{\sigma_{ys}}$ of 11 ksi was intermediate to AA 6061 and the other 2xxx series alloys. Similarly, the $\boldsymbol{\sigma_{uts}}$ for AA 6061 was roughly 30% to 50% lower than the other alloys. The 2xxx series alloys exhibited similar $\boldsymbol{\sigma_{ys}}$ and $\boldsymbol{\sigma_{uts}}$ properties, with AA 2219 and AA 2043 exhibiting lower $\boldsymbol{\sigma_{uts}}$ and AA 2043 exhibiting lower $\boldsymbol{\sigma_{ys}}$ as well. Plate product forms from AA 2050 and AA 2139 offer the largest $\Delta\boldsymbol{\sigma_{form}}$ (~23 ksi) – difference between $\boldsymbol{\sigma_{ys}}$ and $\boldsymbol{\sigma_{uts}}$ - as an indication of work hardening capacity. AA 2043 recorded a $\Delta\boldsymbol{\sigma_{form}}$ of ~18 ksi, ~20% lower than AA 2050 and AA 2139 plate. Meanwhile the $\Delta\boldsymbol{\sigma_{form}}$ for AA 6061 (both plate and forging), AA 2050 and AA 2219 forgings was roughly 50% of the AA 2050 and AA 2139 plate.

3.1.2 Tensile Ductility

The ductility in tension was noticeably higher in AA 6061 and AA 2139 compared to AA 2050 and AA 2219 in the -O temper condition. Specifically, e_u (elongation during stable deformation, i.e., prior to necking) was 17-19% for AA 6061 and AA 2139. However, e_u was lower in AA 2050, AA 2043, and AA 2219, generally 14% to15% with the lowest observed for AA 2050 forging (10%). Similarly, the e_t values were highest in AA 6061 and AA 2139, at roughly 28% to 35%. AA 2050, AA 2043 and AA 2219 recorded lower e_t values, ranging from 13% to 20%. Both AA 6061 and AA 2050 L/A orientations exhibited increased e_u and e_t in the plate vs. rolled ring forging product form. These metrics remained constant for the T/C orientations. AA 6061 and AA 2050 forgings exhibited over 20% higher e_u and e_t in the T/C orientation than L/A orientation while there was no difference in these metrics for AA 2219 forging. The increase in these metrics for AA 6061, AA 2139, and AA 2050 plates were 2% to 10% and were lower by about 15% for AA 2043 billet.

Among the alloys tested, AA 6061 provided the highest ***AR***, with a value of 59% for plate and 49% for forged product in the L/A orientations. AA 2139 plate provided ~38% ***AR***, AA 2050 was measured at 26% for plate and 34% for forged product, and the lowest ***AR*** was measured in AA 2043 at ~15%. Results for the T orientation show similar trends for most of the other alloys and product forms. Notably, AA 6061 rolled ring forging provided ~10 percentage points higher ***AR*** in the C orientation, indicating greater ductility in this orientation. Also notable, AA 2050 exhibited higher ductility and ***AR*** in the rolled ring forging versus plate for both A and C orientations.

3.1.3 Strain Hardening Exponent

The highest ***n*** values were computed for AA 2139 plate, AA 2050 plate, and AA 2043 billet, at 0.29, 0.26, and 0.27, respectively. AA 6061 products exhibited slightly lower ***n*** values with an exponential value of ~0.23 to 0.24. Rolled ring forgings for AA 2219 and AA 2050 demonstrated the lowest ***n*** values with a value of 0.16 to 0.17 in the axial orientations, nearly half of the value for AA 2139, AA 2050 plate products and AA 2043 billet. The ***n*** values for the axial orientation of the rolled ring forgings were approximately half that of the circumferential orientation. These values may indicate that the rolled ring forgings have poor formability in the axial orientation, which is not desirable for flow forming. Strain hardening is implicitly related to both $\Delta\sigma_{form}$ and e_u. As observed, the trends in $\Delta\sigma_{form}$ and e_u agree with the computed ***n*** values for each alloy, with AA 2139 and AA 2050 plate products performing superior to AA 6061 and 2219. AA 2043 billet did not follow this trend, which may reflect differences in the cast microstructure compared with wrought plate microstructure. While there was a reduction in ***n*** values for the AA 2050 plate product vs. forging, AA 6061 displayed comparable ***n*** values for both plate and forging.

The Considère criterion is an established relationship between strain hardening exponent and the onset of necking, i.e., e_u [34]. In general, necking initiates when the true strain exceeds the ***n*** value, i.e., $e_u \geq n$. However, for 2xxx series alloys evaluated in the -O temper condition, this criterion was not satisfied, indicating that necking originates earlier than expected. AA 6061 was the only alloy tested in the -O temper where the ***n*** and e_u values are approximately equivalent. In addition, the strength coefficient, ***K***, generally correlates with strength. The ***K*** values are lowest for AA 6061 and highest for AA 2139 and AA 2050.

3.1.4 Strain Energy

Two parameters based on strain-energy, μ_r and μ_t, were used to assess the capability of each alloy/temper/product form combination to accommodate elasto-plastic deformation. The μ_r value indicates the capacity of a material to absorb energy *elastically*, while the μ_t measures the capacity to absorb energy from *both elastic and plastic deformation*. The μ_r values were highest for AA 2050 forging at 0.017 ksi. The μ_r was roughly 0.01 ksi for the other 2xxx series

alloys, AA 2139, AA 2050 (plate), and AA 2219, which was roughly three times that of AA 6061 (0.003 ksi). The measured μ_r for AA 2043 was ~50% of that reported for the majority of the other 2xxx series alloys.

Some studies have identified correlations between the μ_r and elastic spring-back during bend testing [36]. These results suggest that AA 6061 would exhibit the lowest degree of elastic spring-back during forming compared to the 2xxx series alloys with AA 2050 likely providing the highest degree of spring-back. Previous reports suggest that high μ_r and ***n*** values worked in concert to improve formability by limiting the pile-up of plasticized material ahead of the roller [25]. The nature of the forming mechanism may dictate whether high or low μ_r is more desirable. For example, lower μ_r may be more desirable for spin formability to limit spring-back, whereas high μ_r may be desirable in flow forming to improve material flow ahead of the roller.

Given the μ_r value is indicative of the elastic strain energy, μ_r may not be sufficient to characterize formability, which is inherently plastic in nature. Therefore, the total strain energy, μ_t, was also computed for each test. When comparing μ_t values, AA 2139 absorbs the most strain energy per unit volume of the alloys considered. AA 2139 plate (7.2 ksi) absorbs 2x the energy of AA 6061, AA 2219 and AA 2050 forgings (~3.5 ksi); AA 2043 billet (3 ksi); and ~50% more than AA 2050 and AA 0601 plate (~5 ksi), implying that AA 2139 offers a formability advantage. The forging and billet products yield significantly lower μ_t than plate. Surprisingly, AA 6061 ranked near the bottom, despite being regarded as a highly formable alloy for flow forming operations.

3.1.5 Plastic Strain Ratio

Typically, the ***r*** value is provided as a single value representing the average of three values corresponding to two orthogonal directions and a 45° orientation measured at a single strain value [30]. However, examining the evolution of the ***r*** value for individual directions with increasing strain may be more useful for formability. Hence, plots of the ***r*** value as a function of strain are provided in Figure 6 for the longitudinal orientation and in Figure 7 for the transverse orientation. Plotting ***r*** values as a function of strain represents a departure from the traditional reporting and calculation of ***r*** values.

Plots of the ***r*** values as a function of tensile strain are provided for the L/A orientations in Figure 6 for the -O temper. The ***r*** values were highest for AA 2043, rising to ~0.85 before tapering off to ~0.75 near failure. The average decay in the ***r*** values for AA 2043 occurred at a rate of -0.007 per 1% tensile strain. The second highest ***r*** values were recorded for AA 2139, peaking at 0.8 and falling to 0.6 just prior to failure. The slope of the ***r*** value for AA 2139 also showed the steepest decay, at a rate of -0.007 per 1% tensile strain. Values for AA 2219 ranged from 0.6 to 0.5, decreasing at rate of -0.006 per 1% tensile strain. Decreasing ***r*** values less than unity indicate preferential thinning in the thickness direction of the tensile specimens (short-transverse direction for plate and radial direction for rolled ring forging and billet). ***R*** values are linked to anisotropy and texture. Therefore, the decreasing ***r*** values likely highlight texture-induced anisotropy and/or localization.

In the L/A directions, AA 6061 and AA 2050 demonstrated the lowest ***r*** values of the alloys tested for both plate and forged product forms. AA 6061 forging decreasing at a rate -0.005 per 1% tensile strain, while AA 6061 plate did not show significant decay with increasing strain. AA 2050 plate ***r*** value decreased at -0.002 per 1% increase in tensile strain, whereas AA 2050 forging ***r*** value demonstrated no decrease with increasing strain. For this data, the alloys with the highest ***r*** values also show the greatest rate of decrease with increasing strain, while the alloys with the lowest ***r*** values show the least change with increasing strain. For formability, ***r*** values that are near 1 and stable are most amenable to an isotropic material response.

Similarly, the ***r*** values are plotted in Figure 7 for the T/C orientations. The ***r*** value for all alloys was higher in the T/C orientations than in the L/A orientations. Interestingly, AA 2219 provided the highest ***r*** value just above 1.0 and falling to 0.8 at failure at a rate of -0.011 per 1% increase in strain. AA 2043 peaked quickly at ~0.85 and decreased sharply to ~0.45 at a failure strain of ~13%. AA 2139 values were similar to the L orientation, ranging from just below 0.8 to 0.6, decreasing at a rate of -0.007 per 1% increase in strain. The similarity in the ***r*** values for the L and T orientations indicates that AA 2139 has greater isotropy and thus will likely deform more uniformly, which is desirable. Once again, AA 2050 and AA 6061 plate and forging were lower than other alloy/product forms, although the curves demonstrated greater spread than for the L/A orientation. AA 6061 forging decreased at a rate of -0.006 per 1% increase in strain, while AA 6061 plate was relatively constant with increasing strain. Similarly, AA 2050 plate decreased at a rate of -0.006 per 1% increase in strain, whereas AA 2050 forging displayed minimal change with increasing strain.

3.2 -T4 Temper Condition

Flow forming in the -T4 temper is beneficial to commercial practice, despite being regarded as less formable than the -O temper condition. A primary advantage is eliminating the need for SHT and quenching after forming, which minimizes distortion for large, thin-walled structures. A secondary advantage is the simpler infrastructure required to perform lower temperature heat treatment without quenching of large articles.

Representative engineering stress-strain curves from -T4 temper specimens are shown in Figure 8 for each alloy/product form. The -T4 temper provided increased strength compared to the -O temper for all alloys, as expected. AA 2139, AA 2043, and AA 2050 offered significantly higher strength than AA 6061. AA 6061 is the only alloy evaluated in multiple product form in the -T4 temper: plate and forging. The ductility for AA 6061 plate (>30%) was notably higher than for forged product (~20%). However, most of the plate products, including AA 2139, and AA 2050 exhibited comparable ductility to the -O temper plots. In contrast, AA 2043-T4 cast billet showed significantly greater ductility in the -T4 temper than in the -O temper.

The absence of the PLC effect in the material response is noteworthy for the stress-strain curve for AA 2139-T4. Some instability was observed in the AA 2050-T4 stress-strain curve during necking. It is unclear if this is attributed to plastic instabilities that occur during necking or PLC effects. Significant serrated flow was found in AA 2043-T4, which is likely problematic for forming in the -T4 temper. The lack of PLC in the AA 2139-T4 temper and significant reduction for AA 2050-T4 is a beneficial sign for formability, particularly at room temperature.

3.2.1 Tensile Strength

In the -T4 temper, AA 6061 remained the lowest strength material with a σ_{ys} of ~18 ksi and an σ_{uts} of ~36 ksi with little difference between plate and forging. The σ_{ys} and σ_{uts} for AA 60601 are both are approximately 50% of the σ_{ys} and σ_{uts} for AA 2139 and AA 2050. The 2xxx series alloys AA 2050 and AA 2139 exhibited similar σ_{ys} and σ_{uts} properties of ~40 ksi and ~60 ksi, respectively. However, AA 2043 was 5-10 ksi lower for σ_{ys} and σ_{uts} in comparison. AA 2139, AA 2043, and AA 2050 provided the largest $\Delta\sigma_{form}$ (~22 ksi), meanwhile the $\Delta\sigma_{form}$ for AA 6061 was roughly 25% lower. The $\Delta\sigma_{form}$ for AA 2139 and AA 2050 in the -T4 temper was nearly identical to that for the -O temper. However, AA 6061 showed a significant increase in the $\Delta\sigma_{form}$ from 10 ksi for the -O temper to 17.5 ksi for the -T4 temper. AA 2043 showed a slight increase in the -T4 temper.

3.2.2 Tensile Ductility

Tensile ductility was noticeably higher in AA 2139 compared to AA 6061, AA 2043 and AA 2050 in the -T4 temper condition. Uniform elongation was ~18% for AA 6061 for plate and

forging, nearly identical to that of the -O temper. AA 2050-T4 and AA 2043-T4 produced slight increases to 19% and 17%, respectively, compared to ~14% in the -O temper. Most interesting of all, AA 2139-T4 resulted in e_u of 24% compared to 17% in the -O temper.

The e_t values were highest in AA 2139 at roughly 34%, which is an increase of 25% from the -O temper condition. AA 2050-T4 and 2043-T4 also yielded increases in e_t by 10% and 33%, respectively, compared to the -O temper. AA 2050, AA 2043, and AA 2139 e_u values exceed the ***n*** value, indicating no premature necking. However, the Considère criterion was not satisfied for AA 6061. AA 6061 demonstrated a reduction in e_t for both plate and forging in the -T4 temper compared with he -O temper. The decrease in the plate e_t for AA 6061-O compared to AA 6061-T4 was ~ 10%. However, the drop was more significant in the forging from 28% in the -O temper to 20% in the T4 temper – a decrease of ~30%. AA 6061-T4(?) plate yielded ~50% greater e_t compared to the forging in the L/A orientations but was about 10% lower in the T/C orientations. The increased ductility in AA 2139-T4, AA 2043-T4 and AA 2050-T4 is surprising and positive indicator for formability in the -T4 temper for 2xxx series alloys.

The greatest ***AR*** was measured in the L orientation for AA 6061 and AA 2139 plate at 49% and 44%, respectively. AA 6061 forging, AA 2050 plate, and AA 2043 billet recorded 33%, 24%, and 25% ***AR***, respectively, for the L/A orientations.

3.2.3 Strain Hardening Exponent

AA 6061 in both plate and forging recorded the highest ***n*** value of the alloys tested in the -T4 temper at ~0.23, roughly 50% higher than AA 2139, AA 2043, and AA 2050 (~0.16). The ***n*** value for AA 6061 was virtually unchanged for -T4 versus -O for both plate and forging. However, the ***n*** values for AA 2139, AA 2043 and AA 2050 were roughly 50% lower than the values reported for the -O temper condition. The drop in ***n*** values for AA 2139, AA 2043, and AA 2050 are associated with higher e_u values in the -T4 temper, which will lower the slope of the work hardening portion of the stress-strain curve. Conversely, AA 6061 e_u values were unchanged from -O to -T4, while the $\Delta\sigma_{form}$ increased. These factors give rise to an increase in the slope of the work hardening region of the stress-strain curve, thereby increasing the ***n*** value.

Similar to the -O temper results, the strength coefficient, ***K***, in the -T4 temper is highest for AA 2139 and AA 2050 and lowest for AA 6061. This trend directly correlates with differences in strength observed for these alloys.

3.2.4 Strain Energy

Since the T4 temper offers higher σ_{ys}, the μ_r value will be higher for all the alloys tested compared to the -O temper. The μ_r value of AA 6061-T4 forging increased to 0.014 ksi compared to 0.003 ksi for the -O temper, while the AA 6061-T4 plate increased to 0.020 ksi from 0.004 ksi for the -O temper. Similarly, the μ_r value of AA 2139-T4 and AA 2050-T4 are ~ 0.08 ksi compared to 0.009 ksi for the -O temper. Due to the higher σ_{ys} for AA 2139 and AA 2050, these two alloys provide 5-6x higher μ_r than AA 6061 in the -T4 temper. Similarly, AA 2043-T4 provided increased μ_r compared to the -O temper by a factor of 10x.

AA 2139-T4 recorded the highest μ_t of 17.8 ksi. The -T4 temper provides an increase of ~2.5x over AA 2139-O due to the higher σ_{ys} and e_u in the -T4 temper. AA 2050-T4 and AA 2043-T4 were ~ 40% to 50% lower than AA 2139-T4 due to lower tensile elongation in both alloys. However, in comparison to AA 2050-O, AA 2050-T4 returned an increase of 2x in μ_t. Likewise, AA 2043-T4 exhibited a 3x increase in the μ_t compared to the -O temper. The μ_t value for AA 6061-T4 forging was computed to be 5.1 ksi, which was the lowest of the alloys investigated in the -T4 temper. The second lowest μ_t was measured for AA 6061-T4 plate at 8.6 ksi. The μ_t

value for AA 6061-T4 increased 1.5x and 1.8x compared to that of AA 6061-O for forging and plate, respectively.

3.2.5 Plastic Strain Ratio

The ***r*** values for the T4 temper in the L orientation are plotted in Figure 9. Overall, the ***r*** value trends for -O and -T4 tempers were similar, except for AA 6061 forging. Since the ***r*** values are associated with anisotropy, this is likely indicative of similar crystallographic texture between -O and -T4 product forms. AA 2043 exhibited the highest ***r*** values in this orientation, similar to the -O temper results. AA 2043-T4 ***r*** value peaks just above 0.8 and decreased to 0.7 with a negative slope of -0.007 per % strain, very similar to AA 2043-O. The ***r*** value for AA 2139 peaks at 0.8 and declines just below 0.6 prior to failure, with a negative slope of -0.006 per % strain, very similar to the values and trend for -O temper plate. AA 6061 forging falls in between plate products for AA 6061, AA 2050, and AA 2139, ranging from 0.6 to 0.5, reflecting an increase in n values from the -O temper. AA 6061 forging declines at an identical rate to AA 2139 of -0.006 per 1% increase in strain. Plate products for AA 6061 and AA 2050 recorded the lowest ***r*** values, ranging from 0.4 to just above 0.3, similar to the -O temper. The ***r*** values for AA 2050 and AA 6061 plate were more consistent with increasing strain than the AA 2139 plate and AA 6061 forging, with an average negative slope of -0.003 per % strain.

The ***r*** values for the -T4 temper in the T orientation are plotted in Figure 10. Both the highest and lowest ***r*** values were observed for AA 6061 forging and plate, respectively, ranging from 0.9 to 0.3. AA 6061 forging ***r*** values decreased with the steepest slope at a rate of -0.016 per % strain at high strain levels, while AA 6061 plate were relatively unchanged with increasing strain. AA 2139, AA 2043, and AA 2050 produced similar values to one another. AA 2043 peaked at ~0.82 and declined to ~0.7 at rate of -0.006 per % strain. AA 2139 ranged from 0.8 to just below 0.6, whereas AA 2050 ranged from ~ 0.7 to 0.6. Both AA 2139 and AA 2050 ***r*** values decreased at a rate of -0.007 per % strain, which was roughly half the rate of decrease for AA 6061.

4. Discussion

NASA has extensive rotary forming experience with AA 6061 from development of the ISC process. Preform materials in the fully-annealed, -O temper, condition have consistently provided the best formability in prior flow forming trials on all scales. However, other candidate alloys provide significant performance benefits over AA 6061 for aerospace applications. An ideal replacement alloy would exhibit formability that meets or exceeds that of AA 6061-O (benchmark), while offering higher strength and improved damage tolerance. The 2xxx series alloys examined in this study are strong candidates for commercial aircraft and launch vehicles. In addition to alloy and temper selection, the product form is governed by the scale of the flow-formed article. Flat plate preforms are not practical for large-diameter applications because a significant effort would be devoted to conversion into the 'starting' cylindrical configuration required for flow forming. However, plate material may be appropriate for spin forming of domes, and spin/shear forming of bulkheads on a large-scale [37,38].

4.1 Formability Metrics for Candidate Alloys

All the 2xxx series alloys included in the current testing program exhibited higher $\boldsymbol{\sigma_{ys}}$ and bigger $\Delta\boldsymbol{\sigma_{form}}$ than AA 6061. A broader $\Delta\boldsymbol{\sigma_{form}}$ provides a wider margin for plastic forming between the initial yield (onset of plastic flow) and the strength limits of the material ($\boldsymbol{\sigma_{uts}}$). A narrow $\Delta\boldsymbol{\sigma_{form}}$ is undesirable, as the small difference in stress between initial material flow and catastrophic failure creates tight margins for forming. AA 2050 and AA 2139 plate in both tempers provided the highest $\boldsymbol{\sigma_{ys}}$ and $\boldsymbol{\sigma_{uts}}$ along with greatest $\Delta\boldsymbol{\sigma_{form}}$ of the alloys/product forms examined. AA 2043-T4 $\Delta\boldsymbol{\sigma_{form}}$ was comparable. The $\boldsymbol{\sigma_{ys}}$, $\boldsymbol{\sigma_{uts}}$, and $\Delta\boldsymbol{\sigma_{form}}$ for AA 2050 and AA 2139 are ~2x those for AA 6061 for both -O and -T4 tempers. Consequently, the ***n*** value for these alloys in the

-O temper also exceeds that for AA 6061. Higher ***n*** values are associated with higher formability and are thus desirable. The softer starting condition for the O temper and strong work hardening response leads to higher ***n*** values than the T4 temper, generally.

High values of both tensile elongation and reduction of area have proven to be pertinent indicators of good flow formability. Specifically, high $\boldsymbol{e_u}$ is a significant metric for gaging formability, as this parameter measures the material ductility up to the onset of necking. Ideally, forming must occur in a stable plasticity regime, avoiding plastic flow localization. In addition, the correlation between ***AR*** and the tube spinnability of a metal (i.e., the maximum reduction in thickness per pass in shear spinning) is well established in the literature [11, 39]. The tube spinnability for both shear and flow forming processes has been shown to be similar for metals with ***AR*** ≥ 50% able to sustain thickness reductions up to 80% in a single pass [39]. The prior correlation between ***AR*** and reduction per pass in flow forming lends credence to this being a key metric for formability. Thus, ***AR*** may be a metric to determine the maximum bite per pass for a given alloy/product form/temper. Many of the alloys investigated produced ***AR*** values less than 50%, indicating the maximum bite per pass will be lower than 80%.

AA 6061 plate and forging in the -O temper exhibited the greatest $\boldsymbol{e_u}$, $\boldsymbol{e_t}$, and ***AR***. with slightly reduced values for AA 2139. Consistently, AA 2139, AA 2050, AA 2043, and AA 2219 in the -O temper exhibited values ~20-50% lower than AA 6061. However, in the -T4 temper, AA 2139 plate outperformed all other alloys examined regarding $\boldsymbol{e_u}$ and $\boldsymbol{e_t}$, while AA 6061 plate offered slightly greater ***AR***. Surprisingly, AA 2139, AA 2050, and AA 2043 offered increased $\boldsymbol{e_u}$ and ***AR*** values in the -T4 temper over the -O temper, which was not found for AA 6061, particularly in the forging. This suggests that formability may be better for 2xxx series alloys in the -T4 temper than the -O temper, which has positive implications for manufacturing operations as most fuselage skin candidate alloys are from the 2xxx series.

A practical indicator of good flow formability is the minimum build-up of material ahead of the advancing rollers during the incremental deformation process [25]. This phenomenon, also referred to as ‘pile-up’ or ‘bow wave’ formation, is often associated with less than adequate formability, excessive defect creation and premature failure [40]. In terms of tube spinning parameters, build-up increases with reduction per pass and feed rate, but decreases with roller tilt angle and nose radius [41]. Reports on flow forming of steels suggest that higher $\boldsymbol{\mu_r}$ values, working in concert with ***n***, prevent accumulation ahead of the rollers and promote material movement along the mandrel axis [15]. Therefore, the possibility that $\boldsymbol{\mu_r}$ and $\boldsymbol{\mu_t}$ values derived from tensile testing may be exploited to gauge the elasto-plastic behavior of candidate materials is worth pursuing. The $\boldsymbol{\mu_r}$ value, a measure of elastic strain energy, relates to elastic spring-back and residual stresses [22,36,42]. Higher $\boldsymbol{\mu_r}$ was found for AA 2050 and AA 2139. The $\boldsymbol{\mu_r}$ metric was greater in the -T4 temper material than in the -O temper for the same alloys.

Alternatively, the high $\boldsymbol{\mu_r}$ values for AA 2050 and AA 2139 may lead to increased elastic spring-back during spin forming. This suggests that these alloys may perform less well than AA 6061 for spin forming, but may perform better for flow forming. Material is more likely to flow axially rather than accumulate in front of the advancing roller. Accordingly, spring-back will be of greater concern for preform materials in the -T4 temper than the -O temper, due to the higher $\boldsymbol{\mu_r}$ values. The differences in spring-back and material movement ahead of the roller will likely require adjustment of the processing variables from alloy to alloy, or from temper to temper within the same alloy. Likewise, the $\boldsymbol{\mu_t}$ value was consistently highest for AA 2139 and AA 2050 compared to AA 2219, AA 2043, and AA 6061, suggesting greater capacity to absorb strain energy and improved flow formability.

One implication of using μ_r as a formability metric within a given alloy system (similar or equivalent ***E***), is that higher strength tempers will provide higher μ_r and thus be considered more formable. The correlation between μ_r and formability appears counterintuitive as ductility/formability is generally inversely related to strength. The μ_t at least factors elongation/ductility into the calculation by considering the total area under the curve. Hence, it may offer better correlation with expected formability for similar alloys that vary by strength and/or temper. These aspects warrant further examination of the relative importance of μ_r and μ_t when ranking of formability.

The ***r*** values were consistently the closest to unity in the L/A orientation for AA 2043 and AA 2139. However, the ***r*** values showed greater decline with increasing strain in AA 2043, which raises the issue of stability during forming. Typical ***r*** values for AA 2139 ranged from 0.8 to 0.6, regardless of temper or orientation. In the T/C orientations, AA 2219 and AA 6061 forgings provided ***r*** values closer to 1, particular at lower strains, in the -O and -T4 tempers, respectively. However, these alloys and AA 2050 displayed lower ***r*** values in the L/A orientations, which is indicative of greater plastic anisotropy. High ***r*** values indicate less thinning in the thickness orientation of the test specimens, which generally correlates to higher formability. AA 2050 and AA 6061 plate consistently produced lower ***r*** values, but with less reduction in the ***r*** values with increasing strain. Consistent ***r*** values may be beneficial for stable forming, whereas larger ranges in the ***r*** value as a function of strain may cause instability as flow forming progresses.

Interestingly, AA 2219-O forging is not always the poorest performer in some of the formability metrics presented in the data, though often it is either the worst or second worst. While it certainly ranks lower in formability, there exists the possibility that the poor flow forming trails noted in [24] may have been partly to blame on forming parameters that were not sufficiently optimized to yield a successful flow formed part. Comparison of the forming data in this paper and subsequent forming trials must keep this possibility in mind with current and future candidate alloys.

4.2 PLC Effects and Implications

The stress-strain curves reveal that all alloys exhibited PLC behavior in the -O temper, with the greatest effect observed in the 2xxx series alloys. Such serrated behavior is a concern from a formability standpoint, due to the higher risk of shear localization in a PLC band and premature failure [43]. The PLC effect is often influenced by strain rate and temperature, but Al alloys are predominantly strain rate insensitive at RT. Some reports have shown that the PLC effect was present in the stress strain curves for an AA 2007 over a range of strain rates [44]. This suggests that the strain rate range may be less critical when flow forming Al alloys at RT. Interestingly, the PLC effect reportedly decreases at lower temperature, indicating that cold forming (below RT) may result in higher tensile ductility and better formability [34], despite being contrary to the typical behavior of decreasing ductility at lower temperatures. The PLC effect is linked to necking at lower strains, which would be characterized in tensile data as lower e_u values. Indeed, the Considère criterion was violated for 2xxx series alloys in the -O temper, where lower than expected e_u values were measured when compared to the onset of necking suggested by the ***n*** value.

The stress-strain curves also reveal that the PLC effect is sensitive to the alloy temper condition. The difference between the -O and -T4 temper for the candidate alloys is conveyed in Figure 11. Most alloys tested exhibited reduced or no PLC effects in the -T4 temper compared to the -O temper (except for AA 2043), which is consistent with other published results. Consequently, the -T4 temper may be a promising material condition for forming of 2xxx series alloys. For example, the PLC effect has been documented in a common fuselage skin alloy, AA 2024, which exhibited less plastic instability in the -T4 versus -T351 temper [45]. Diffusion of solute atoms in the -T4 temper is slowed due to the trapping of solute atoms in the stress fields

around Guinier-Preston (GP) zones [46]. The absence or reduction of the PLC effect in the -T4 temper is likely associated with the lower diffusion rates.

A separate study for Al-Li alloys noted that formation of the δ' (Al_3Li) phase and the associated promotion of planar slip may lead to strain localization and reduced ductility in -T4 [47]. AA 2043 contains 1.6 wt.% Li, roughly 60% more Li than AA 2050. The increased Li would favor more precipitation of δ' in the -T4 temper as a result of natural aging [48]. Planar slip due to shearing of δ' may explain the PLC effects observed in AA 2043-T4. This effect may be reduced by forming in a temper where δ' precipitates are absent, such as the -W temper.

PLC behavior, which is often correlated with solute-dislocation interactions, should be more prevalent in Al alloys with higher solute content. In this case, the PLC effect was indeed more prominent in the 2xxx series alloys (containing 3-6 wt.% Cu) than AA 6061 (containing 1 wt.% Mg). The solute content of the matrix should also be higher in the -T4 temper than the -O temper because (GB) precipitation is maximized and the solute content of the matrix minimized in the latter condition. On this basis, the PLC effect should be more prevalent in the substantially stable condition (-T4 temper) than the equilibrium condition (-O temper). However, the data presented (Figure 5 and Figure 8) do not support either of these hypotheses and suggest that metastable phases (such as GP zones) may play a vital role.

4.3 Formability Rankings

A ranking system was adopted to provide a more tangible outcome from this work and provide insight. These over-simplified rankings are based on individual formability metrics, whereas a balance between metrics is actually required. Plus, these metrics likely exhibit an interdependency that will necessitate elaborate ranking schemes in ongoing studies. The formability rankings (average of both orientations) of the candidate alloy/temper/product combinations evaluated are different, based on whether ***AR***, ***n***, $\boldsymbol{\mu_r}$, r, or $\boldsymbol{\mu_t}$ is employed as the discriminating metric.

Table 7 provides ranking of formability metrics ***AR***, ***n***, and $\boldsymbol{\mu_r}$ separated by product form for the relevant alloy/temper combinations. This presentation clearly highlights the improved performance for the plate products forms. Within the plate product forms AA 6061 and AA 2139 consistently outperform AA 2050. In the two cylindrical product forms (forging and billet), AA 6061 and AA 2050 offers higher ***AR***, while AA 2043 is more favorable for ***n***, and $\boldsymbol{\mu_r}$.

As an alternative method of evaluating the formability metrics, Table 8 identifies the top three alloy/temper combinations based on ***AR***, ***n***, $\boldsymbol{\mu_r}$, r, and $\boldsymbol{\mu_t}$ irrespective of product form. AA 6061 was not considered in this ranking since the emphasis is on fuselage candidates and AA 6061 offers poorer service properties compared to the 2xxx series alloys. AA 6061 is included as the benchmark for ranking flow formability. Of the 2xxx series alloys, AA 2139 is the best all-around performer.

- When ***AR*** is selected, AA 2139-T4 (P), 2139-O (P) and AA 2050-O (F) are ranked #1, #2, and #3.
- When ***n*** is selected, AA 2139-O (P), AA 2043-O (B), and AA 2050-O (P) are ranked #1, #2, and #3.
- When $\boldsymbol{\mu_r}$ is selected, AA 2139-T4 (P), AA 2050-T4 (P), AA 2043-T4 (B) are ranked #1, #2, and #3.

As noted, AA 2139 (P) ranks highly in both the -O and -T4 tempers. In the case of AA 2139-T4 (P), ***AR*** is lower (44.1 vs. 54.5 %), ***n*** is lower (0.163 vs. 0.232), and $\boldsymbol{\mu_r}$ is much higher (0.082 vs. 0.003 ksi) than the benchmark AA 6061-O (F), when averaged over L/A and T/C orientations.

The ***r*** values are < 1 for most of the materials evaluated, which is indicative of preferential thinning in the radial or short-transverse direction of the test specimen, depending on product form. In general, the ***r*** value gradually decreases with increasing strain, indicating progressively more anisotropic deformation under tensile loading.

- In the case of AA 2139-T4 (P) for the L orientation, the ***r*** value decreases from a max. of 0.78 at 4.0 % strain to a min. of 0.57 at 33.6 % strain. Compared with the benchmark AA 6061-O (F) for the A orientation, the ***r*** value decreases from a maximum of 0.48 at 2.0 % strain to a minimum of 0.33 at 27.8 % strain. Thus, 2139-T4 plate shows less anisotropy than the benchmark 6061 forging, suggesting better performance with respect to ***r***.
- In the case of AA 2139-T4 (P) for the T orientation, the ***r*** value decreases from a maximum of 0.78 at 4.5 % strain to a minimum of 0.56 at 32.4 % strain. Compared with the benchmark AA 6061-O (F) for the C orientation, the ***r*** value decreases from a maximum of 0.65 at 1.0 % strain to a minimum of 0.44 at 35.3 % strain. Again, 2139-T4 shows less anisotropy than the 6061-O (F) benchmark in the transverse orientation.

The formability rankings (average of both orientations) of the candidate alloy/temper/product combinations evaluated are different, based on whether ***r*** or μ_t is employed as the discriminating metric.

- When maximum ***r*** value is selected, AA 2043-O (B), AA 2043-T4 (B), and AA 2139-O (P) are ranked #1, #2, and #3.
- When maximum μ_t value is selected, AA 2139-T4 (P), AA 2050-T4 (P), AA 2043-T4 (B) are ranked #1, #2, and #3.

In the case of AA 2139-T4 (P), maximum ***r*** is higher (0.78 vs. 0.57) and μ_t is much higher (17.3 vs. 2.3 ksi) than the benchmark AA 6061-O (F), when averaged over the L/A and T/C orientations.

The ***r*** value is closer to unity for nearly all the candidate alloy/temper/product combinations than the benchmark material, AA 6061-O (F), i.e., more isotropic tensile deformation. The -O vs. -T4 data comparisons for a particular alloy plate product reveal that the ***r*** value is unaffected by temper condition. The plate vs. forging data comparisons for all candidate materials do not show a trend between plastic anisotropy and product form. The strain-dependent ***r*** value becomes more important when forming ISCs, because plastic anisotropy will play a role in complete stiffener formation.

The μ_t value indicates the level of elastic and plastic strain energy that can be accommodated before failure. In this study, the materials with the highest ***AR*** values (key metric) are AA 6061-O (benchmark), AA 2139-T4, and AA 2139-O, with corresponding μ_t values of 3.4 ksi, 17.8 ksi, 7.2 ksi, indicating that a correlation with formability is not evident. Therefore, the results are inconclusive with regards to the significance of the μ_t value. It may be speculated that μ_t exerts an influence on build-up ahead of the roller similar to the effect of μ_r, the elastic equivalent.

The tensile data related to AA 6061 and AA 2050 indicate that product form exerts an influence on flow formability, with plate offering superior ductility to rolled ring forgings. Additionally, the AA 2043 data suggest that conventionally cast product forms may provide the least ductility. The test results also reveal that temper condition exerts a comparable influence on flow formability. The -O temper generally provides the greater ***n*** and ***AR*** values, whereas the -T4 temper provides the larger μ_r and μ_t values. However, materials in the -O temper appear susceptible to the PLC effect, which will degrade formability. Continuation of VUD-600 forming trials should elucidate the best balance between these metrics, and guide temper selection for maximum formability. It is also accepted that flow forming of plate preforms is impractical for large-scale applications. Hence, subscale trials utilizing plate preforms likely represent an upper bound for formability based on superior performance to other product forms evaluated. As a result, scale-up efforts

may encounter lesser formability in thick-walled rings comprised of forgings, extrusions, or castings. The use of alternate product forms may require specialized processing to boost the formability of preform materials to an acceptable level.

5. Concluding Remarks

AA 2139 emerges as the most promising fuselage candidate, due to an attractive combination of high formability of plate in the -T4 temper and potential service performance. AA 2139 was in the top three ranked materials for all formability metrics and -T4 plate the top-ranked for the majority of the metrics. Forming AA 2139 in the -T4 condition is encouraging from the perspective of obtaining service properties in flow-formed material via simple heat treatments. The major implication for full-scale ISC structures is that a balance between strength and damage tolerance may be achieved through direct (low temperature) aging practices. Reports indicate that AA 2139 rolled product can exhibit -T8 properties in a traditional -T6 temper condition, i.e., no cold stretch [22]. The capability of reaching peak strength levels without cold working is attractive for manufacturing of complex-shaped, thin-walled structures. In contrast with many alloys, where strength comes at the expense of damage tolerance, Reports show that AA 2139-T8 sheet also has excellent fatigue resistance and fracture toughness [14].

Conducting flow forming trials on large preforms without knowing which 2xxx Al alloys have sufficient formability is not the best use of material resources. The solution is to employ smaller tensile specimens, and apply published testing and analysis protocols to multiple materials. The goal is to screen and rank the formability of candidate aerospace alloys to assist with forming trials. In addition to the recommended metrics $\boldsymbol{AR}$, $\boldsymbol{n}$, or $\boldsymbol{\mu_r}$, the values of $\boldsymbol{r}$ and $\boldsymbol{\mu_t}$ are also visited. The use of tensile testing to assess flow formability is well established, but applying DIC to bulk, rather than sheet, forming may be creative. However, using the approach to differentiate between the responses of Al alloys in different temper conditions and product forms *is* innovative.

The results generated by this study highlight two uncertainties that will be resolved by continuing R&D. First, the formability metrics from tensile testing adopted were originally applied to flow forming of steels [19]. However, forming trials on Al alloy plate preforms involve a dynamic change from spin to flow form deformation. Second, spin/flow forming involves high, variable strain rates and large plastic strain. In contrast, tensile testing involves lower, constant strain rates and much less plastic strain. Thus, VUD-600 operations will need to confirm the efficacy of each formability metric derived from tensile data for ranking of candidate Al alloy products. Comparison of forming trial results with the tensile data reported in this study will identify the balance of metrics that correlate with the best flow formability and provide for a hierarchical ranking scheme.

6. Future Considerations

Extensive spin/flow forming trials on the aerospace Al alloy materials evaluated in this study will be planned. The formability metrics reported will be correlated with the process variables derived from forming trials to validate the screening methodology. These trials will include high-ranked alloy/temper/product combinations and exploration of additional candidate materials. Only the best parameters for flow forming of an AA 6061-O preform into a fully-formed, defect-free component will be documented from ISC fabrication. Identifying parameters leading to a high probability of success for new alloy/temper/product form combinations will be critical for the forming trials to be effective. Otherwise, some candidates may be regarded as having poor flow formability when inappropriate processing variables could actually be the culprit; a distinct possibility for AA 2219.

This initial study presented in this Technical Publication (TP) was guided by a literature review related to material parameters considered important for formability in spin/flow forming. The current state of the art indicated that when using classical tensile testing, the modulus of resilience, work hardening coefficient, and tensile reduction of area are the three that appear to contribute most significantly to formability and are used as material screening metrics [25, 39, 41]. Bylya, et al. provided a concise review of and support for these accepted tensile screening metrics as well as an examination of the relationship between work (strain) hardening and true strain for several alloys and stated that strain hardening may be the key metric for flow forming [25]. However, a comprehensive investigation into the rate of work hardening ($\boldsymbol{\theta}$ or $\boldsymbol{d\sigma/d\varepsilon}$) and the effects on the flow or true stress for spin/flow forming has not been reported. A future study into $\boldsymbol{\theta}$ may be productive for formability assessment when evaluated based on the theoretical stages of work hardening and the mechanisms that contribute to deformation. Specifically, differences in the so-called Stage III and IV work hardening response may provide better screening for formability for the alloys, tempers, and product forms of interest. In Stage III, the $\boldsymbol{\theta}$ decreases linearly with respect to the increase in flow stress due to dynamic recovery and is characterized by a saturation stress that marks the transition to Stage IV where the linear relationship does not hold at higher stresses [49]. Many factors influence Stage III, including solute and shearable and non-shearable precipitates. With the interest in forming in a -W or -T4 temper, the effect of solute in solid solution on Stage III hardening may be critical for formability. Solute reduces the rate of dynamic recovery [49]. Additionally, the solute may increase the degree of Stage III hardening. However, a higher strain rate appears to decrease the impact of solute in Stage III [50]. Stage IV behavior is linked to easy glide. Therefore, grain orientation and texture will influence Stage IV hardening. In contrast to Stage III, Stage IV is insensitive to solute effects [49]. Large strain deformation is attributed to extended Stage IV hardening, which is likely critical for high wall thickness reductions and good flow formability [49].

As a result of this study on 2xxx series aluminum alloys, two aspects emerge as worthy of future investigation in connection to the rate of work hardening and formability:

1) The impact of solute and precipitates on Stage III rate of work hardening, and
2) The impact of texture on Stage IV work hardening behavior.

Understanding the interaction of the microstructure may be critical in defining the proper starting condition for enhanced formability in the 2xxx series alloys and for forming parameter optimization. Specifically, one may want to optimize the microstructure to limit the extent of Stage III hardening in favor of enhancing Stage IV response. Furthermore, controlling the transition from Stage III to IV likely requires a variable feed rate during the flow forming process. The work of Teixeira, et al. [50] implies a higher initial strain rate may be required to transition from Stage III to IV. Once in Stage IV, the strain may be reduced to prevent cracking concerns.

It is recognized that Al alloys with lower solute content, such as AA 6061, tend to be more compatible with flow forming operations conducted at RT. However, many of the high-performance Al alloys of more interest originate from the less cold-formable 2xxx-series alloy family. The significant Cu content results in increased strain hardening and renders the candidate alloys susceptible to PLC effects that can reduce formability. Consideration of interactions between the dynamics of processing and changing material conditions could mitigate these effects. As an example, inserting a recovery annealing treatment between spin and flow forming on the VUD-600 might prevent the strain hardening budget from being exhausted, thereby avoiding premature failure.

Further benefits of a recovery annealing treatment may include mitigation of residual stresses. Significant residual stresses may be accumulated during flow forming, given the complex and high level of deformation associated with the desired wall thickness reductions, plus stiffener heights for fuselage structures. Residual stresses pose two problems for fuselage structures:

1) lead to distortion and compromise part fit up during manufacturing; and 2) influence fatigue performance, particularly in the high cycle fatigue regime where aircraft operate. Recently produced 10-ft. diameter AA 6061 ISCs did exhibit some distortion upon post-forming solution treating and quenching [1]. Currently, the residual stresses within an ISC formed part have not been characterized. Future work should seek to quantity the residual stress state within the wall and stiffeners of an ISC, perform a fatigue test to evaluate the effect of residual stresses on the fatigue life of an ISC-produced barrel, and examine processing strategies to mitigate residual stresses, if warranted. Forming in a -T4 temper provides a potential solution to eliminate the distortion risk by avoiding solution treating and quenching. However, a recovery anneal may alleviate residual stress and improve fatigue life.

Plastic anisotropy in the preform material, which depends on product form, will exert an influence on formability. For example, the original reference axes pertaining to the preform change during flow forming of a flat plate into a cylinder. The L orientation transforms to the A orientation at 12 o'clock and 6 o'clock, and the T orientation transforms to the A orientation at 3 o'clock and 9 o'clock. Flow formability in the axial and circumferential directions may vary around the perimeter of the deforming cylinder. Simultaneously, the short-transverse orientation transforms to the radial orientation throughout. Analogous to the earing behavior during deep drawing of Al alloy sheet stock, crystallographic texture does play a role in plastic flow at RT [51]. As a result, the plastic strain ratio, ***r***, will become increasingly important for candidate materials with strong deformation textures, such as unrecrystallized Al-Li alloys. Consequently, the directional properties of commercially available product forms warrant careful consideration in future research.

The primary focus of this study was to establish whether tensile testing combined with DIC can guide parameter selection for VUD-600 forming trials. The formability metrics derived from tensile testing should assist in adaptation of the established forming parameters for AA 6061-O to new candidate materials. For example, evaluating the relative differences may indicate the adjustment direction (increase or decrease) for process variables, effectively compressing the parameter space to be explored. The schematic in Figure 12 indicates the extensive processing-related permutations involved and that taking a machine learning approach should accelerate parameter optimization [52]. A variety of methods will also be evaluated for importing formability metrics into DEFORM® software to facilitate accurate predictions of spin/flow forming behavior [17]. An approach based on integrated computational materials engineering (ICME) should expedite optimization of flow forming variables for high-performance alloys.

Ultimately, the properties of flow-formed barrel sections may represent a trade-off between formability and service performance. The latter will strongly depend on preform microstructure / temper, process variables, and post-forming heat treatment. Damage tolerance is the critical design allowable property for fuselage structures and data covering fracture toughness and fatigue properties of flow-formed Al alloy materials are non-existent. Impact and cyclic testing of a 10-ft-diameter, full-scale article is complex and expensive. A 2-ft-diameter, sub-scale article fabricated on the VUD-600 could be an economical way of generating pathfinder data.

7. References

[1] Tayon, W. A., Rudd, M. T., Marcia Domack S., and Hillburger, M. W., "Development of Advanced Manufacturing Approaches for Single-Piece Launch Vehicle Structures," NASA Technical Memorandum (TM) 20210026743. 2021.

[2] Zell, D., Domack, M., Tayon, W., Stachulla, M., and Wagner, J., "Developments on Low Cost Manufacturing Methods for Cylindrical Launch Vehicle Structures," Presented at the *67th International Astronautical Congress*, 2019.

[3] Tayon, W. A., Domack, M. S., Wagner, J. A., Taminger, K., and Hoffman, E., "Development and Characterization of the Integrally Stiffened Cylinder (ISC) Process for Launch Vehicles and Aircraft Fuselage Structures," *Proceedings of The Minerals, Metals, and Materials Society (TMS) Annual Meeting 2020*, 2020.
[4] Marini, D., Cunningham, D., Xirouchakis, P., and Corney, J., "Flow Forming: A Review of Research Methodologies, Prediction Models and Their Applications," *International Journal of Mechanical Engineering & Technology*, Vol. 7, No. 5, 2016, pp. 285–315.
[5] H.A. Kuhn, "Workability theory and Application in Bulk Forming Processes," *Handbook of Workability and Process Design*, G.E. Dieter, H.A. Kuhn and S.L. Semiatin (eds.), ASM International, Materials Park, OH, 2003, pp. 172-187.
[6] Nägele, H., Wörner, H., and Hirschvogel, M., "Automotive Parts Produced by Optimizing the Process Flow Forming–Machining," *Journal of Materials Processing Technology*, Vol. 98, No. 2, 2000, pp. 171–175.
[7] Anon., "Applications – Chassis & Suspension – Wheels," *The Aluminium Automotive Manual*. https://european-aluminium.eu/blog/aluminium-automotive-manual/. Accessed July 17, 2023.
[8] Roy, M. J., and Maijer, D. M., "Experimental Procedure for Warm Spinning of Cast Aluminum Components," *Journal of Visualized Experiments*, No. 120, 2017, pp. 55-61.
[9] Semiatin, S. L. (ed), *ASM Handbook, 14A. Metalworking: Bulk Forming*. ASM International, Materials Park, OH, 2005. pg. 521.
[10] Dieter, G. E., *Mechanical Metallurgy*, McGraw-Hill, New York, NY, 1986. pp. 554, 652.
[11] Kuhn, H., and Medlin, D., "*Mechanical Testing and Evaluation*," ASM Handbook Vol. 8, ASM International, Materials Park, OH, 2000. Pg. 70.
[12] Chang, S.-C., Huang, C.-A., Yu, S.-Y., Chang, Y., Han, W.-C., Shieh, T.-S., Chung, H.-C., Yao, H.-T., Shyu, G.-D., and Hou, H.-Y., "Tube Spinnability of AA 2024 and 7075 Aluminum Alloys," *Journal of Materials Processing Technology*, Vol. 80, 1998, pp. 676–682.
[13] Brice, C., Shenoy, R., Kral, M., and Buchannan, K., "Precipitation Behavior of Aluminum Alloy 2139 Fabricated Using Additive Manufacturing," *Materials Science and Engineering: A*, Vol. 648, 2015, pp. 9–14.
[14] Cho, A., and Bes, B., "Damage Tolerance Capability of an Al-Cu-Mg-Ag Alloy (2139)," *Materials Science Forum,* No. 519, 2006, pp. 603–608.
[15] Rioja, R. J., and Liu, J., "The Evolution of Al-Li Base Products for Aerospace and Space Applications," *Metallurgical and Materials Transactions A*, Vol. 43, No. 9, 2012, pp. 3325–3337.
[16] Hafley, R. A., Domack, M. S., Hales, S. J., and Shenoy, R. N., "Evaluation of Aluminum Alloy 2050-T84 Microstructure and Mechanical Properties at Ambient and Cryogenic Temperatures," NASA Technical Memorandum (TM) 20160010564, 2016.
[17] Anon., *Aluminum Alloy, Extruded Profiles (2043-T85) 2.8Cu - 1.65Li - 0.35Mg - 0.1Zr Solution Heat Treated, Stress Relieved by Stretching, and Aged*. SAE International, Warrendale, PA, 2019.
[18] Liu, T., Zhan, X., Zhao, Y., Bai, M., and Gong, X., "Study on 2219 Aluminum Alloy T-Joint during Dual Laser-Beam Bilateral Synchronous Welding : Effect of the Welding Speed and Incident Beam Angle on Grain Morphology," *Optics & Laser Technology*, Vol. 119, No. 105594, 2019.
[19] Anon., *Aerospace Material Specification 2770H: Heat Treatment of Wrought Aluminum Alloy Parts*, SAE International, Warrendale, PA, 2010.
[20] Tayon, W., Domack, M., and Wagner, J., "Characterization of 10-Ft. Diameter, Aluminum Alloy 2219 Integrally Stiffened Cylinders," NASA Technical Memorandum (TM) 2019-220260, 2019.
[21] Lankford, W. T., "New Criteria for Predicting the Press Performance of Deep Drawing Sheets," *Trans. ASM*, Vol. 42, 1950, pp. 1197–1232.
[22] Ghosh, A. K., "The Influence of Strain Hardening and Strain-Rate Sensitivity on Sheet Metal Forming," *Journal of Engineering Materials and Technology*, Vol. 99, No. 3, 1977, pp. 264–274.

[23] Firat, M., Kaftanoglu, B., and Eser, O., “Sheet Metal Forming Analyses with an Emphasis on the Springback Deformation,” *Journal of Materials Processing Technology*, Vol. 196, Nos. 1–3, 2008, pp. 135–148.
[24] Meyers, M and Chawla, K., *Mechanical Behavior of Materials*, Cambridge University Press, New York, 2009. pp. 176, 229-230.
[25] Bylya, O. I., Khismatullin, T., Blackwell, P., and Vasin, R. A., “The Effect of Elasto-Plastic Properties of Materials on Their Formability by Flow Forming,” *Journal of Materials Processing Technology*, Vol. 252, 2018, pp. 34–44.
[26] Kegg, R. L., “A New Test Method for Determination of Spinnability of Metals,” *Journal of Engineering for Industry*, Vol. 83, 1961, pp. 119–124.
[27] Urig, E., and Zhigilei, L., “Finite Element Modeling of Plastic Deformation During Spin Forming of Aluminum 6061-O,” *Virginia Space Grant Consortium*, 2023.
[28] Anon., “Designation E8: Tension Testing of Metallic Materials. American Society for Testing and Materials,” *Annual Book of ASTM Standards Vol. 3.01*. West Conshohocken, PA, 2010.
[29] Anon., “Designation E646: Standard Test Method for Tensile Strain-Hardening Exponents (n-Values) of Metallic Sheet Materials,” *Annual Book of ASTM Standards Vol. 3.01*. American Society for Testing and Materials, West Conshohocken, PA, 2010.
[30] Anon., “Designation E517: Standard Test Method for Plastic Strain Ratio r for Sheet Metal,” *Annual Book of ASTM Standards Vol. 3.01*. American Society for Testing and Materials, West Conshohocken, PA, 2010.
[31] Hecker, S. S., “Formability of Aluminum Alloy Sheets,” *Journal of Engineering Materials and Technology*, Vol. 97, No. 1, 1975, pp. 66–73.
[32] Lege, D. J., Barlat, F., and Brem, J. C., “Characterization and Modeling of the Mechanical Behavior and Formability of a 2008-T4 Sheet Sample,” *International Journal of Mechanical Sciences*, Vol. 31, No. 7, 1989, pp. 549–563.
[33] Aleksandrovi, S., Stefanovi, M., Adamovi, D., and Lazi, V., “Variation of Normal Anisotropy Ratio ‘r’ during Plastic Forming,” *Journal of Mechanical Engineering*, Vol. 55, No. 6, 2009, pp. 392–399.
[34] Halim, H., Wilkinson, D. S., and Niewczas, M., “The Portevin–Le Chatelier (PLC) Effect and Shear Band Formation in an AA5754 Alloy,” *Acta Materialia*, Vol. 55, No. 12, 2007, pp. 4151–4160.
[35] Robinson, J. M., “Serrated Flow in Aluminium Base Alloys,” *International Materials Reviews*, Vol. 39, No. 6, 1994, pp. 217–227.
[36] da Silva, É. A., de Siqueira, R. P., Martins, M. S., and dos Santos Pereira, M., “Analysis of the Springback Effect with Respect to Resilience in High-Strength Steels Applied to the Automotive Industry,” Presented at the 22nd International Congress of Mechanical Engineering (COBEM 2013), Brazil, 2013.
[37] Curreri, P., Hoffman, E., Lollar, L., Bank, J., Domack, M., Stewart, T., Edahl, R., Pham, D., Torres, P., Li, T., Shenoy, R., Caratus, A., Reinmuller, R., Russell, C., Crooks, R., Schneider, J., and Tayon, W., “Aluminum-Lithium, Friction Stir Welded, Spun-Formed Domes for Light-Weight Cryogenic Propellant Tanks Part I: 1-Meter-Diameter Proof of Concept,” NASA Technical Publication (TP) 2011216462, 2011.
[38] Domack, M., Hoffman, E., Raju, I., Piascik, R., and Squire, M., “Spin Forming Aluminum Alloy Crew Module (CM) Metallic Forward Pressure Vessel Bulkhead (FPVBH) – Phase I,” *NASA* NASA Technical Memorandum (TM) *2014-218163*, 2014.
[39] Kalpakjian, S., *Manufacturing Processes for Engineering Materials*, Pearson Education, New York, NY, 1991. pg. 313.
[40] Sariyarlioglu, E. C., Music, O., and Bakkal, M., “Backward Tube Spinning Mechanics,” *The International Journal of Advanced Manufacturing Technology*, Vol. 123, Nos. 1–2, 2022, pp. 479–491.
[41] Kalpakjian, S., and Rajagopal, S., “Spinning of Tubes: A Review,” *Journal of Applied Metalworking*, Vol. 2, 1982, pp. 211–223.

[42] Xue, P., Yu, T. X., and Chu, E., “An Energy Approach for Predicting Springback of Metal Sheets after Double-Curvature Forming, Part I: Axisymmetric Stamping,” *International Journal of Mechanical Sciences*, Vol. 43, No. 8, 2001, pp. 1893–1914.

[43] Benallal, A., Berstad, T., Børvik, T., Hopperstad, O. S., Koutiri, I., and de Codes, R. N., “An Experimental and Numerical Investigation of the Behaviour of AA5083 Aluminium Alloy in Presence of the Portevin–Le Chatelier Effect,” *International Journal of Plasticity,* Vol. 24, No. 10, 2008, pp. 1916–1945.

[44] Darowicki, K., Orlikowski, J., and Zieliński, A., “Investigation of Changes in the Type B PLC Effect of Al–Mg–Cu Type Alloy for Various Strain Rates,” *Materials Science and Engineering: A*, Vol. 496, Nos. 1–2, 2008, pp. 478–482.

[45] Gupta, S., Beaudoin, A. J., and Chevy, J., “Strain Rate Jump Induced Negative Strain Rate Sensitivity (NSRS) in Aluminum Alloy 2024: Experiments and Constitutive Modeling,” *Materials Science and Engineering: A*, Vol. 683, 2017, pp. 143–152.

[46] Kang, J., Liu, X., and Wang, T., “The Effects of Ultrasonic Vibration on Portevin–Le Chatelier (PLC) Effect and Stress-Strain Behavior in Aluminum Alloy 2024,” *Scripta Materialia*, Vol. 224, 2023, pp. 115-121.

[47] Dong, F., Yi, Y., Huang, S., Wang, B., He, H., Huang, K., and Wang, C., “Cryogenic Formability and Deformation Behavior of 2060 Al–Li Alloys with Water-Quenched and T4 Aged Temper,” *Materials Science and Engineering: A*, Vol. 823, No. 141722, 2021.

[48] Deschamps, A., Decreus, B., De Geuser, F., Dorin, T., and Weyland, M., “The Influence of Precipitation on Plastic Deformation of Al–Cu–Li Alloys,” *Acta Materialia*, Vol. 61, No. 11, 2013, pp. 4010–4021.

[49] Poole, W. J., Embury, J. D., and Lloyd, D. J., "Chapter 11 - Work Hardening in Aluminium Alloys," *Fundamentals of Aluminium Metallurgy* (R. Lumley, ed.), Woodhead Publishing, 2011, pp. 307–344.

[50] da Costa Teixeira, J., Bréchet, Y., Estrin, Y., and Hutchinson, C., “The Strain Hardening Behaviour of Supersaturated Al-Cu Alloys,” *Proceedings of the 12th International Conference on Aluminum Alloys (ICAA),* 2010.

[51] Hirsch, J., “Texture Evolution and Earing in Aluminium Can Sheet,” *Materials Science Forums*, No. 495, 2005, pp. 1565–1572.

[52] Runge, M., “Spinning and Flow Forming,” *Leifeld GmbH Werkzeugmaschinenbau/Verlag Moderne Industrie AG, D-86895, Landsberg/Lech*, 1994.

[53] Hales, S.J., “In-House Flow Forming of Aluminum Structures: Identifying and Selecting Process Variables,” Internal Presentation to AATT Working Group, NASA Langley Research Center, Hampton, VA, December 15, 2020.

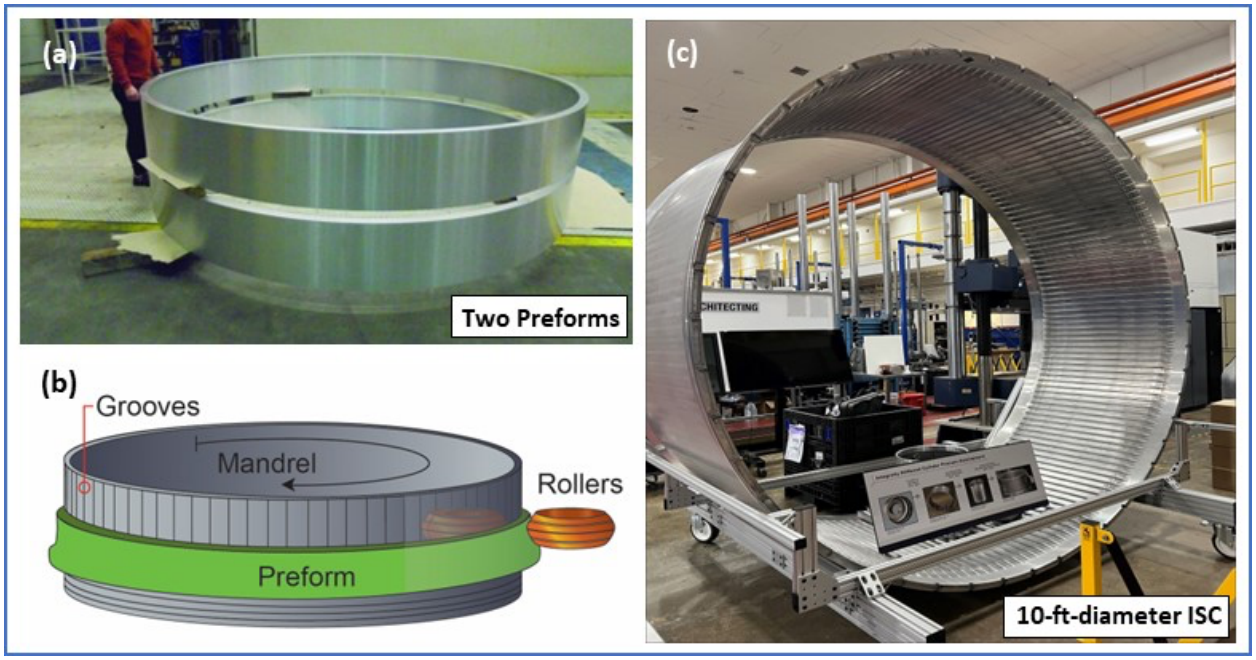

Figure 1. ISC fabrication technology: (a) typical preforms; (b) schematic of process; (c) full-scale barrel section.

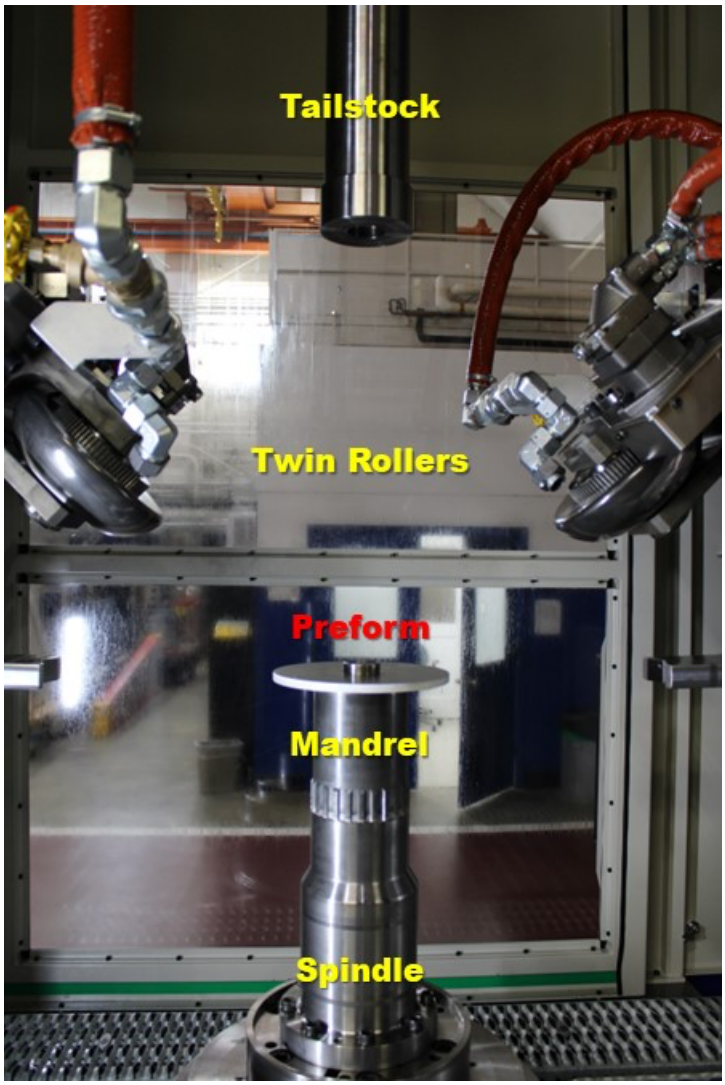

Figure 2. Inner workings of R&D spin/flow forming machine at NASA LaRC.

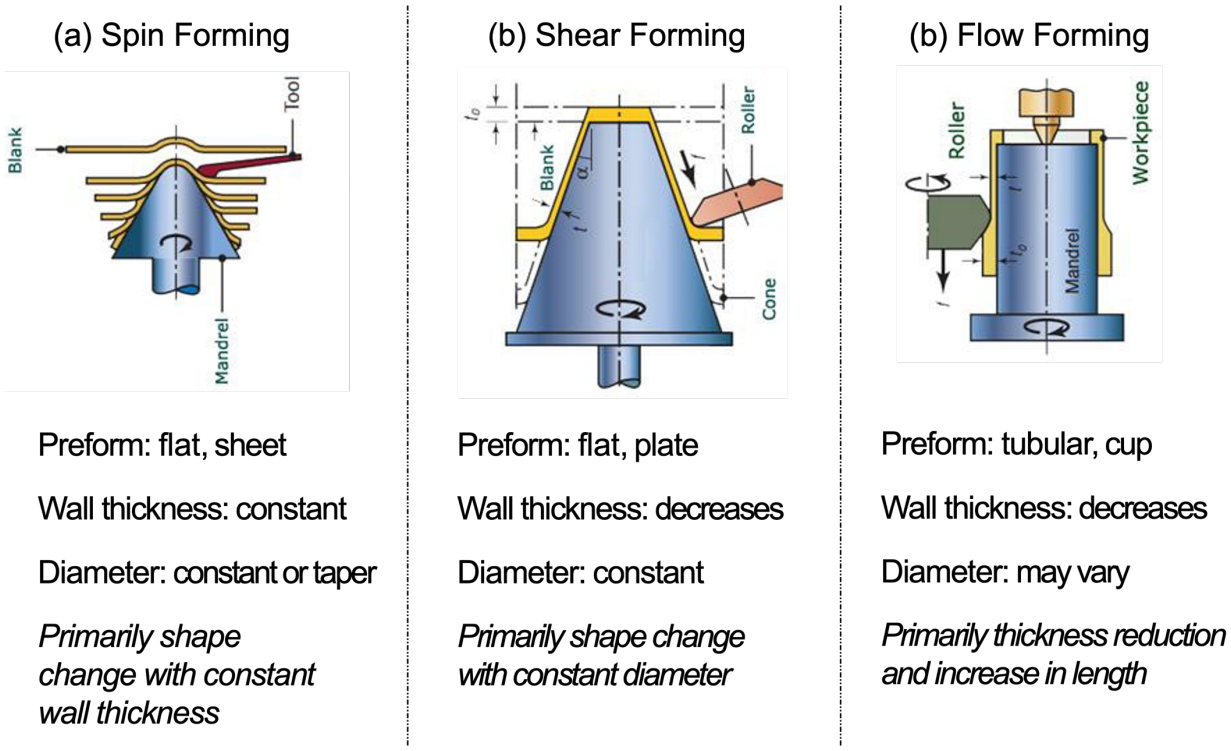

Figure 3. Basic categories of rotary forming processes showing type of incremental deformation [51].

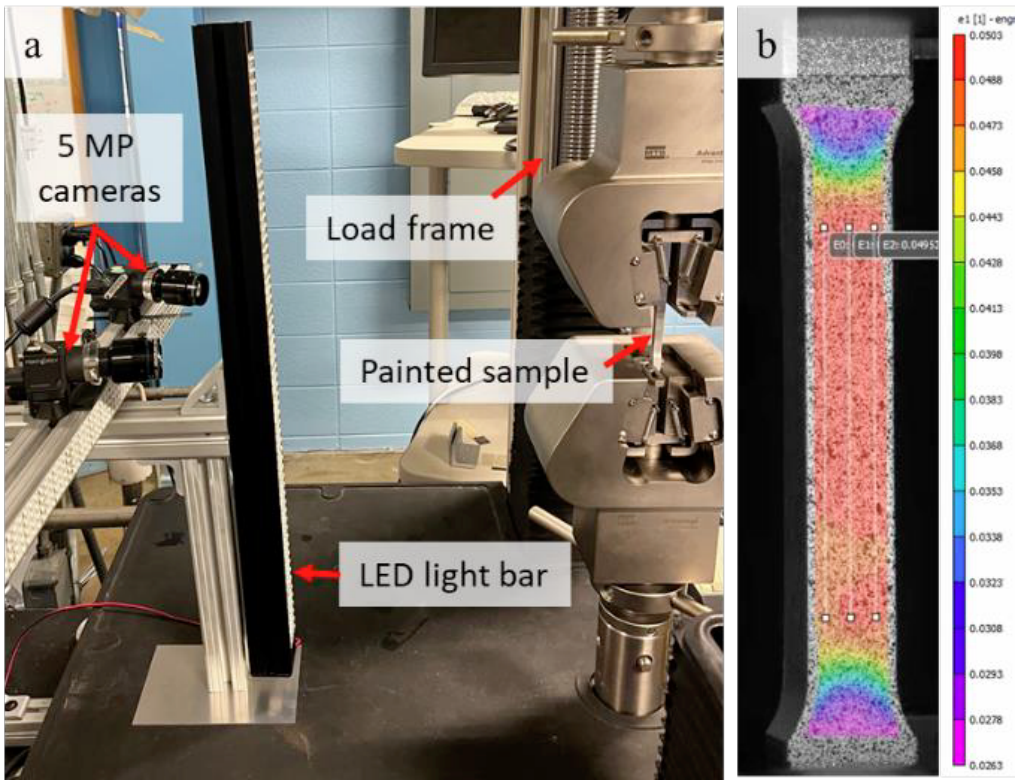

Figure 4. Tensile testing setup: (a) equipment configuration; (b) speckle-painted sample with DIC results displayed at 5% strain.

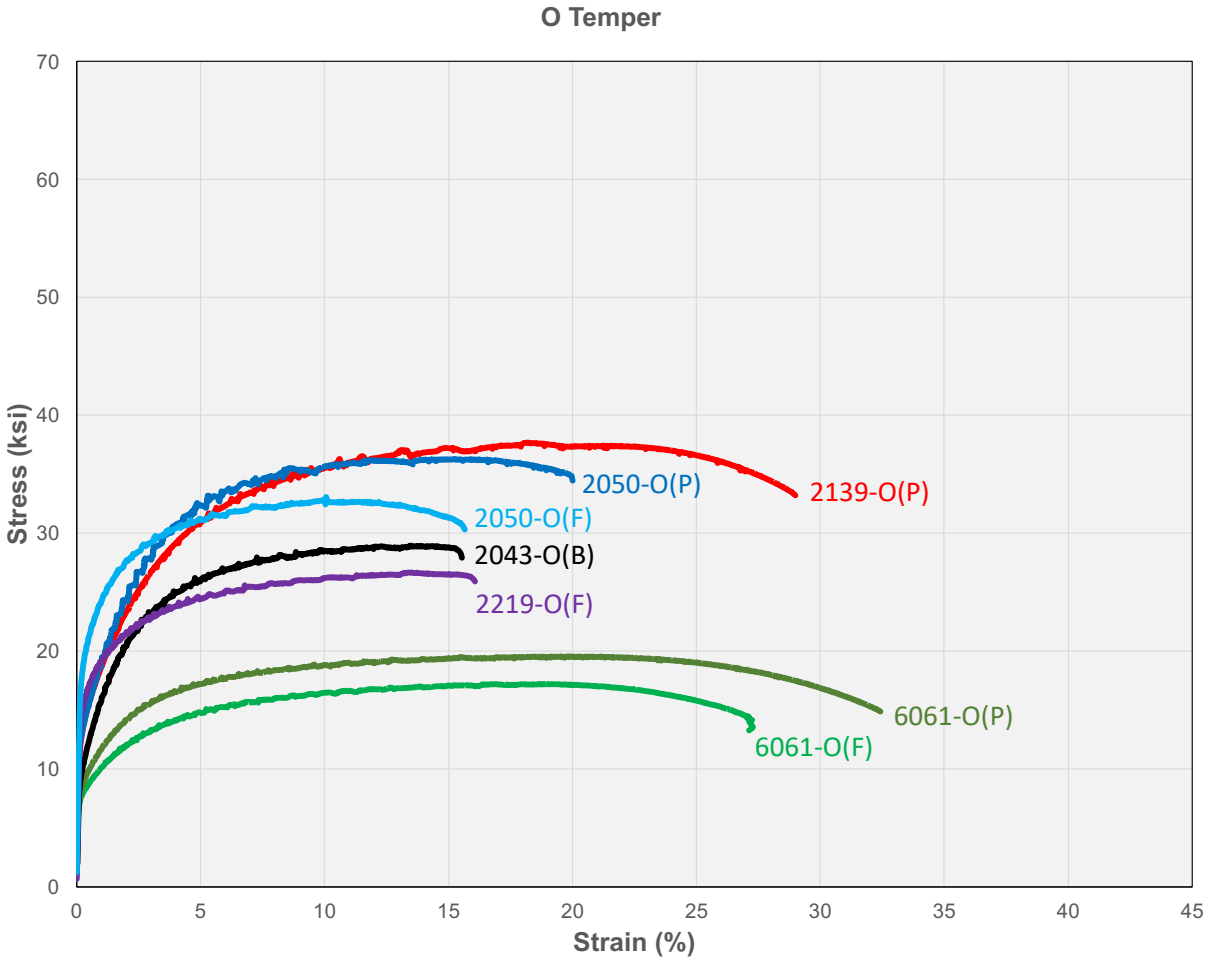

Figure 5. Engineering stress-strain curves for the -O temper.

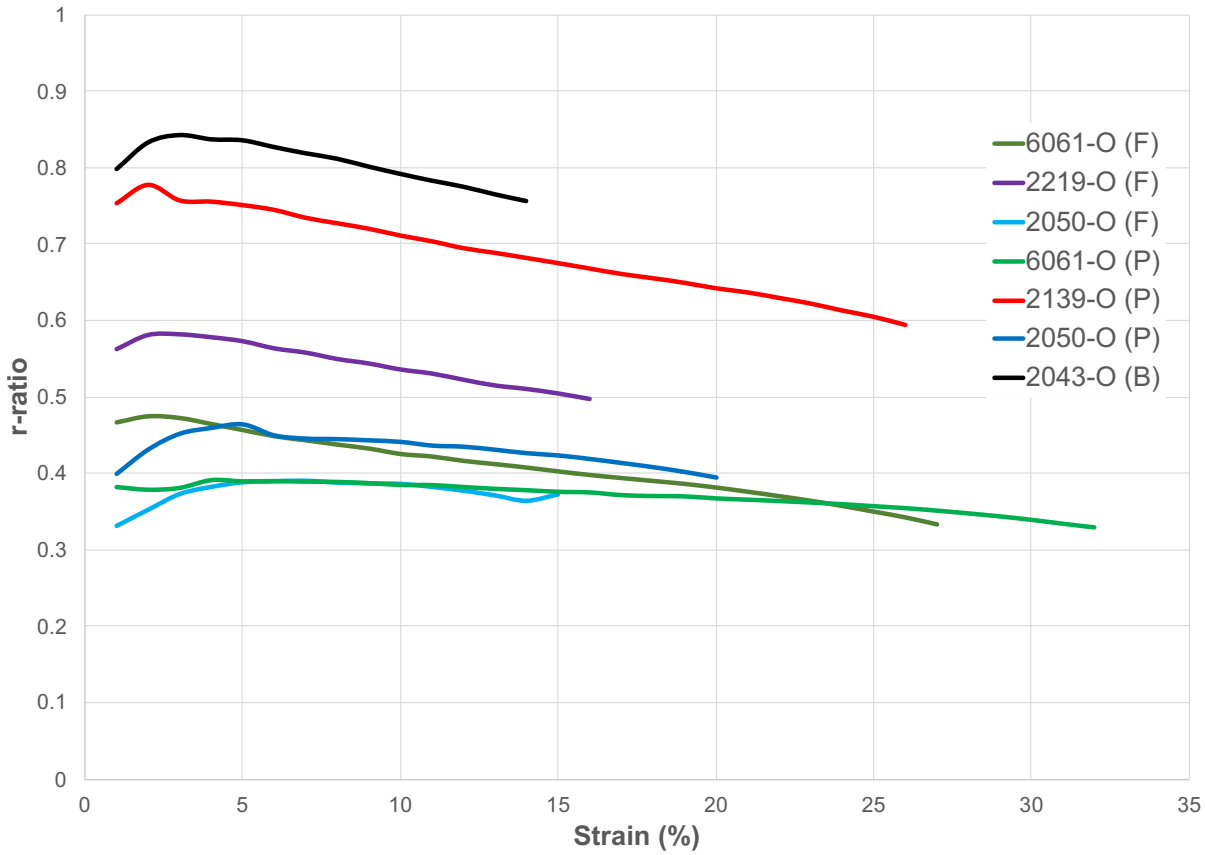

Figure 6. The r value vs. engineering strain for longitudinal/axial orientation in -O temper.

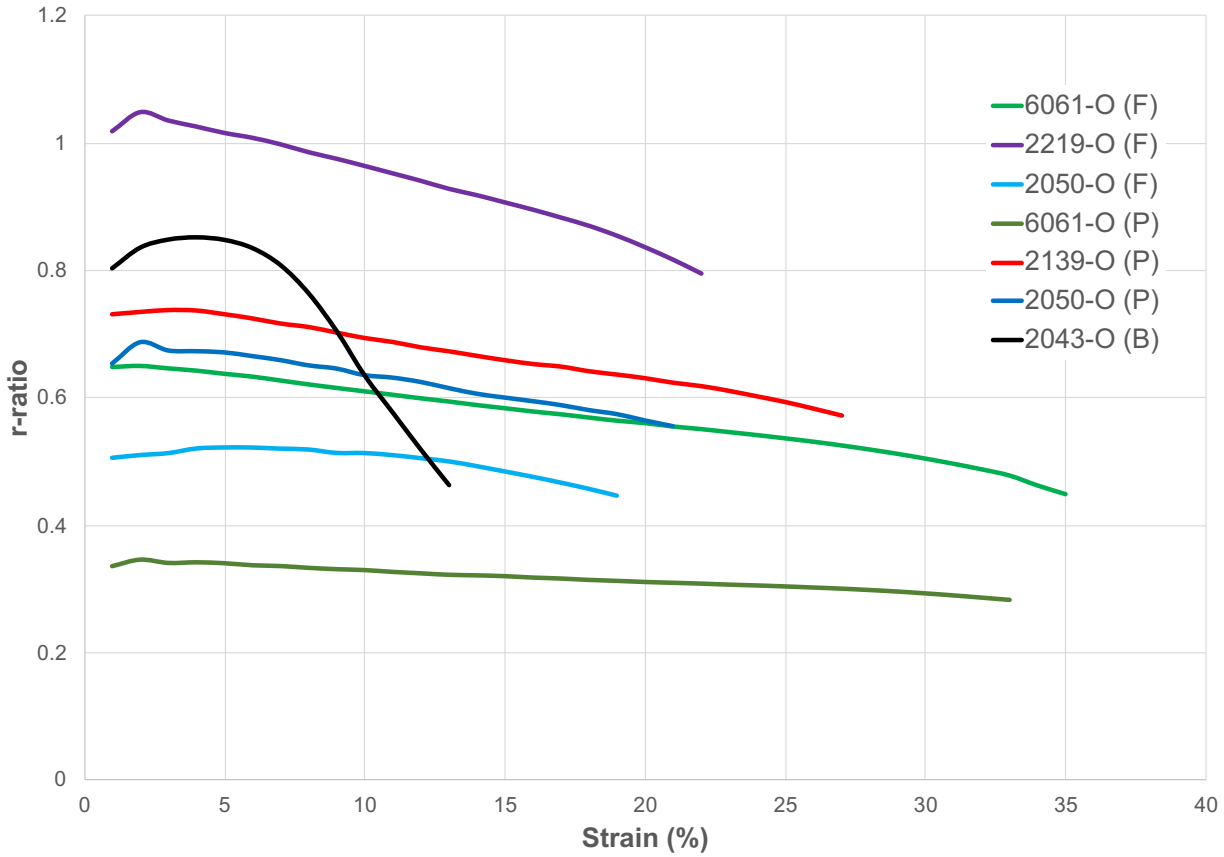

Figure 7. The r value vs. engineering strain for transverse/circumferential orientation in the -O temper.

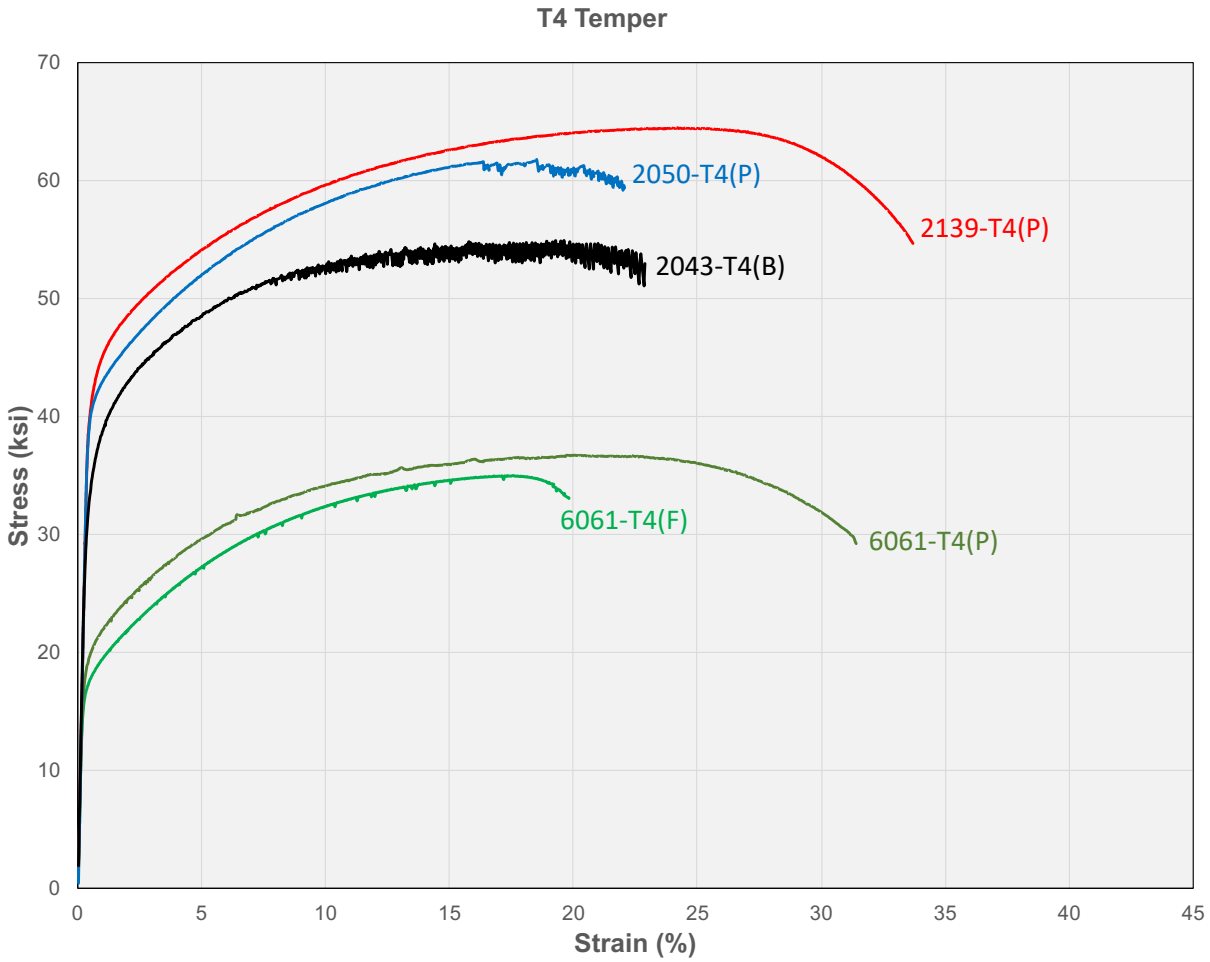

Figure 8. Engineering stress-strain curves for the -T4 temper.

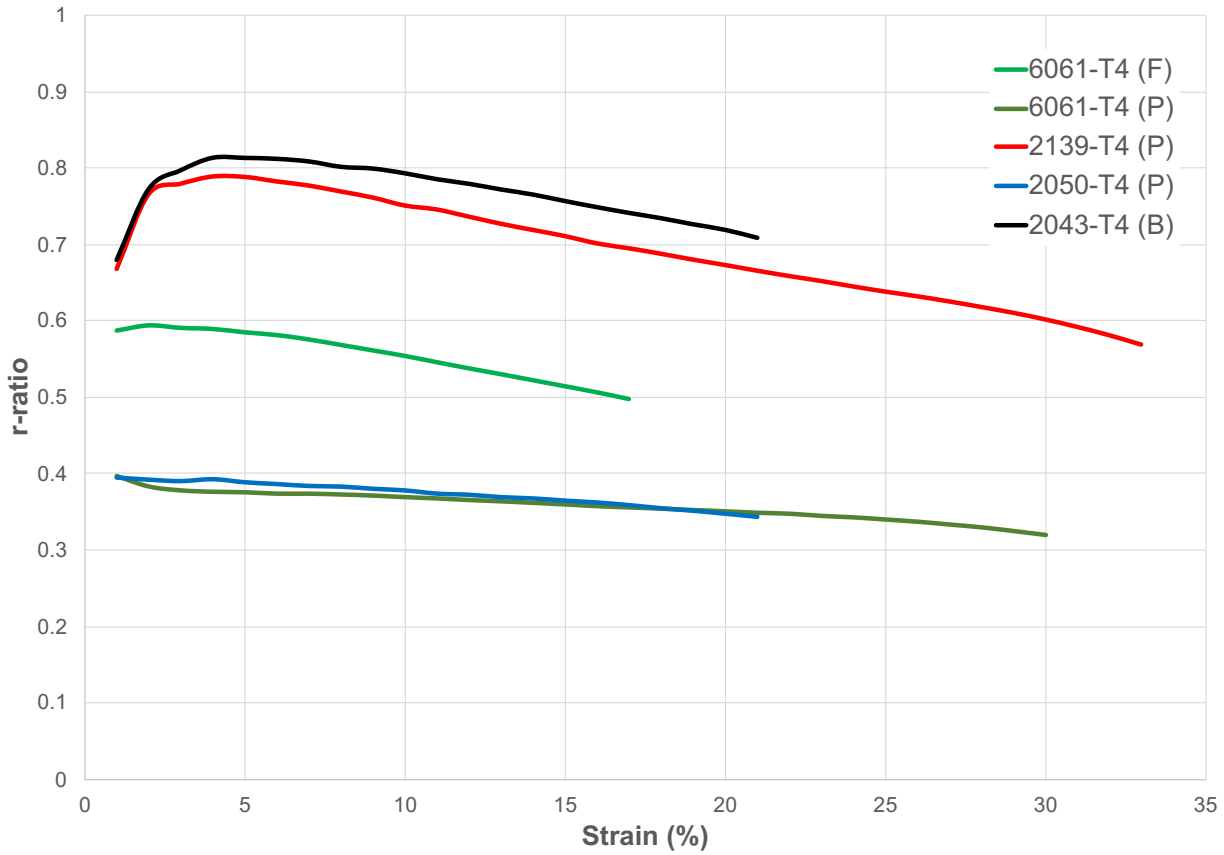

Figure 9. The r value vs. engineering strain for longitudinal/axial orientation in -T4 temper.

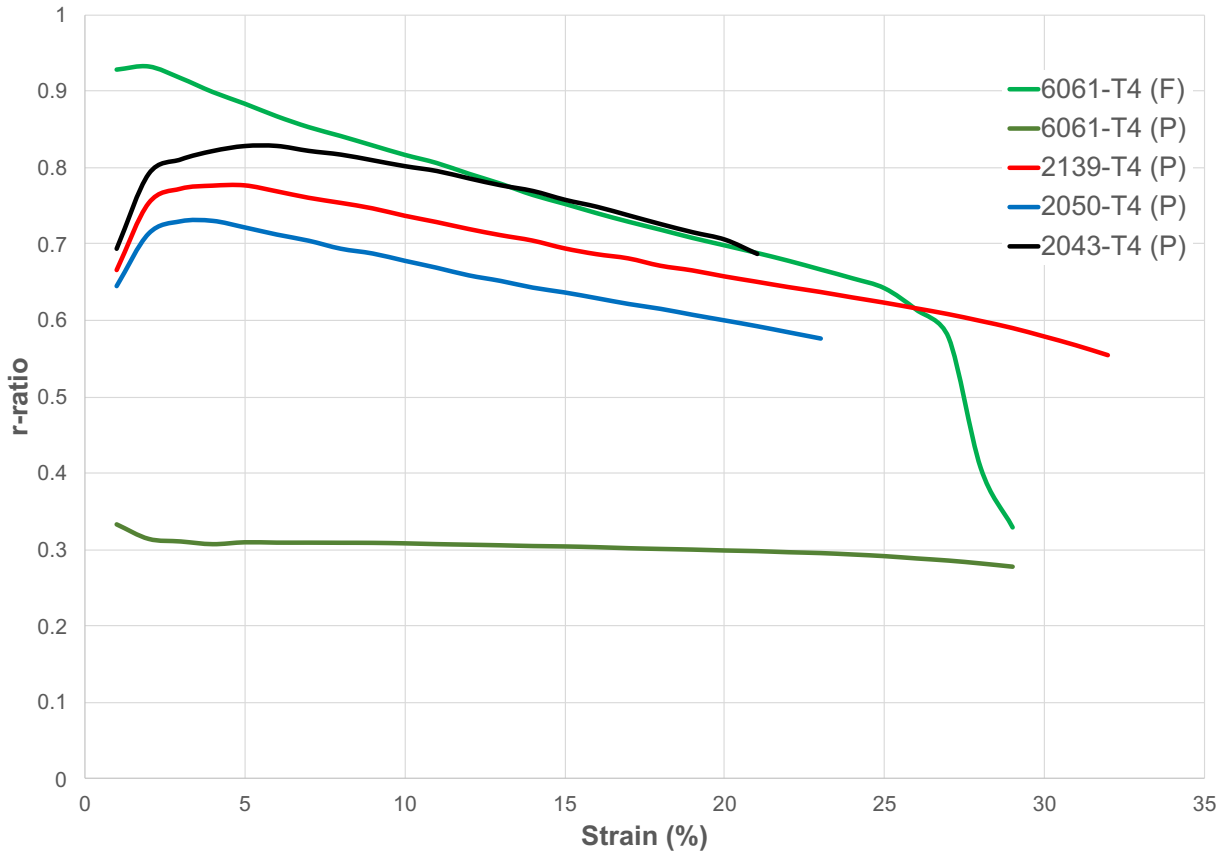

Figure 10. The r value vs. engineering strain for transverse/circumferential orientation in -T4 temper.

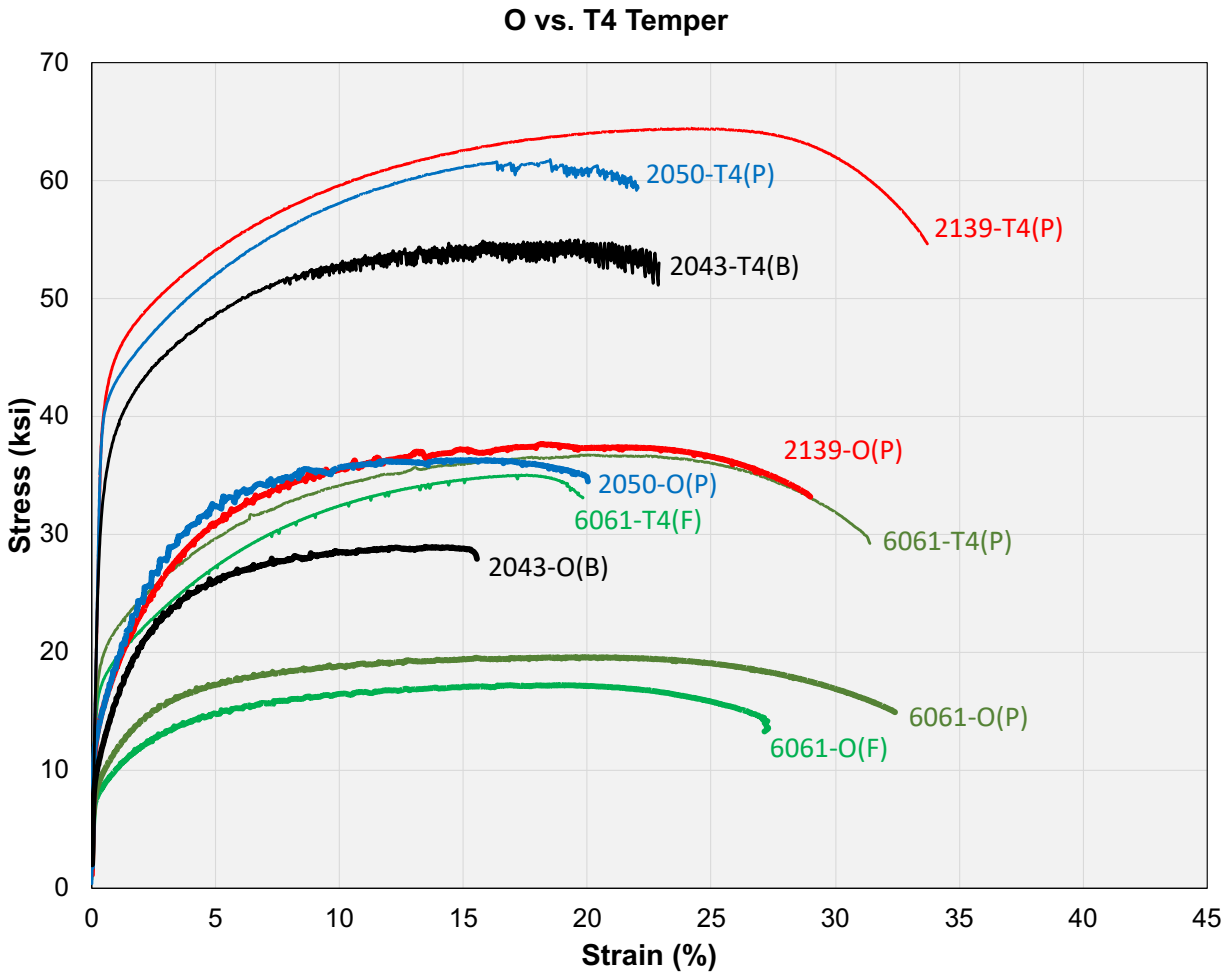

Figure 11. Comparison of -O vs. -T4 temper: engineering stress-strain curves.

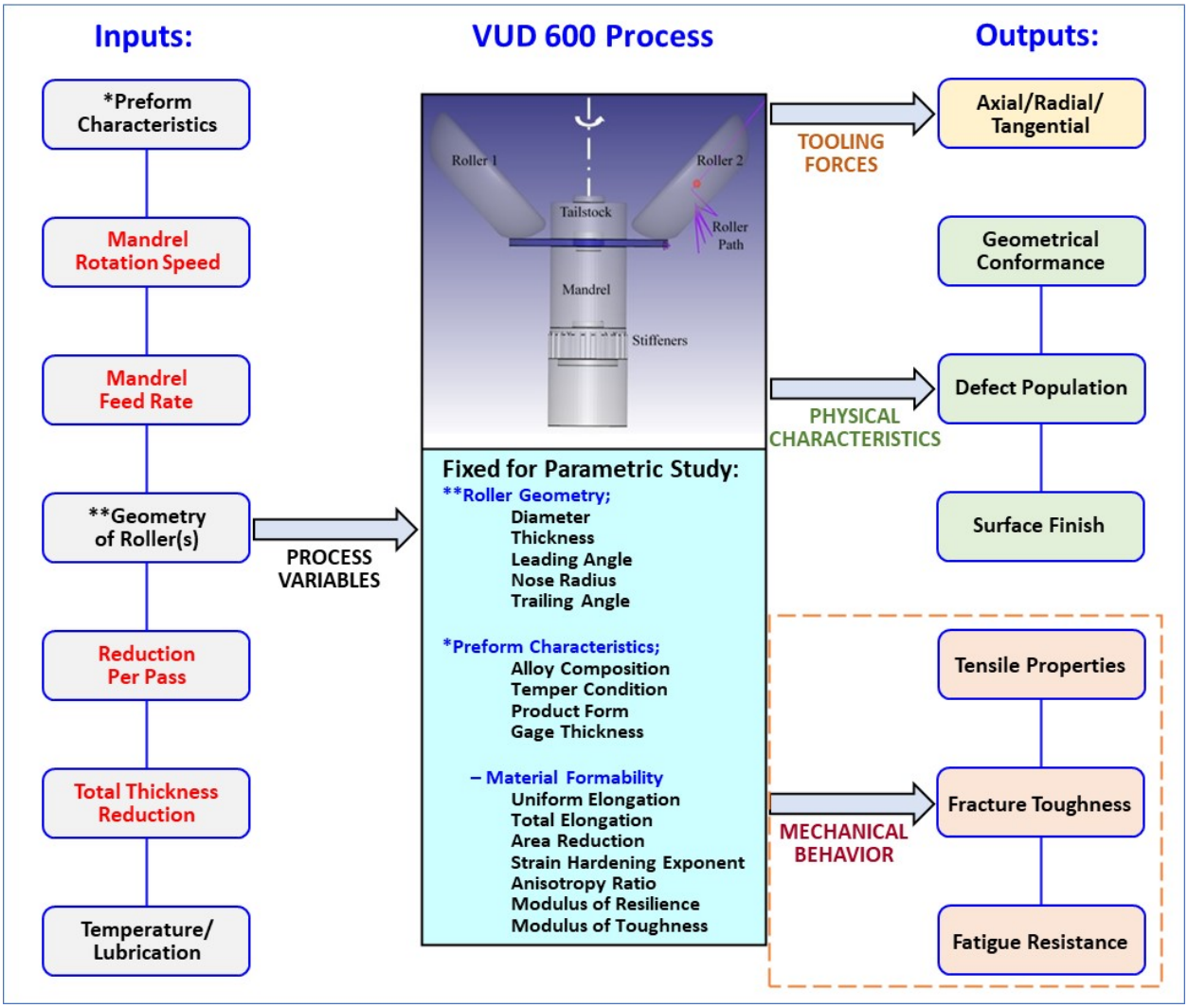

Figure 12. The large number of processing variables associated with VUD-600 forming trials [53].

Table 1. Nominal elemental compositions of Al alloys evaluated (wt. %).

Alloy	Ag	Cr	Cu	Fe	Li	Mg	Mn	Si	Ti	V	Zn	Zr
6061	--	0.2	0.28	<0.7	--	1.0	--	0.6	<0.15	--	<0.25	--
2139	0.4	--	5.0	<0.15	--	0.5	0.4	<0.1	<0.15	<0.05	<0.25	--
2219	--	--	6.3	<0.3	--	<0.02	0.3	<0.2	0.06	0.1	<0.1	0.1
2050	0.4	--	3.6	--	1.0	0.4	<0.5	--	<0.1	0.1	<0.25	0.1
2043	<0.1	--	2.8	--	1.6	0.4	<0.3	<0.08	<0.1	--	<0.3	0.1

***Balance Al. All other elements < 0.05 wt. % each and < 0.15 wt. % total.*

Table 2. Solution heat treatment temperatures for Al alloys evaluated.

Alloy	SHT Temp. (°F)
6061	985
2139	1,004
2219	995
2050	932
2043	1,010

Table 3. Tensile data for longitudinal/axial orientation: -O temper.

Alloy	6061 (F)	6061 (P)	2139 (P)	2050 (F)	2050 (P)	2219 (F)	2043 (B)
σ_{uts} (ksi)	17.1	19.7	37.6	32.1	36.8	26.5	28.9
σ_{ys} (ksi)	7.7	8.9	14.3	19.2	15.1	15.2	11.0
$\Delta\sigma_{form}$ (ksi)	9.4	10.8	23.3	13.0	21.7	11.3	17.9
e_u (%)	17.4	19.4	17.1	9.5	15.4	14.1	14.1
e_t (%)	27.8	33.7	27.9	15.3	19.9	16.6	15.2
AR (%)	49.0	59.2	37.6	33.6	26.1	NM	15.7
K (ksi)	31.4	35.4	77.1	52.4	75.2	43.0	60.4
n	0.238	0.225	0.287	0.161	0.263	0.170	0.268
μ_r (ksi)	0.003	0.004	0.010	0.017	0.011	0.011	0.006
μ_t (ksi)	3.4	4.8	7.2	3.9	5.1	3.5	3.0

NM= not measured

Table 4. Tensile data for transverse/circumferential orientation: -O temper.

Alloy	6061 (F)	6061 (P)	2139 (P)	2050 (F)	2050 (P)	2219 (F)	2043 (B)
σ_{uts} (ksi)	16.9	19.4	37.4	31.8	36.7	27.2	28.9
σ_{ys} (ksi)	7.9	9.4	14.2	15.2	14.4	12.5	10.8
$\Delta\sigma_{form}$ (ksi)	9.0	10.1	23.2	16.7	22.3	14.7	18.1
e_u (%)	22.9	21.2	19.0	13.0	15.6	14.1	12.1
e_t (%)	35.3	34.5	27.7	20.1	21.8	16.6	13.2
AR (%)	60.0	57.1	39.6	37.3	30.9	NM	16.4
K (ksi)	30.0	33.4	76.0	60.7	76.5	51.5	62.0
n	0.226	0.205	0.284	0.232	0.277	0.244	0.274
μ_r (ksi)	0.003	0.004	0.010	0.011	0.010	0.011	0.005
μ_t (ksi)	1.1	5.0	6.0	4.7	5.5	3.1	2.8

NM= not measured

Table 5. Tensile data for longitudinal/axial orientation: -T4 temper.

Alloy	6061 (F)	6061 (P)	2139 (P)	2050 (P)	2043 (B)
σ_{uts} (ksi)	34.5	36.9	64.4	61.9	55.1
σ_{ys} (ksi)	16.9	19.4	42.1	40.9	34.2
$\Delta\sigma_{form}$ (ksi)	17.6	17.5	22.3	21.0	20.9
e_u (%)	16.9	20.0	24.1	18.8	17.2
e_t (%)	19.9	30.8	33.6	21.9	22.0
AR (%)	33.2	49.3	44.2	24.1	25.5
K (ksi)	62.3	64.2	99.1	95.8	84.3
n	0.243	0.224	0.163	0.167	0.154
μ_r (ksi)	0.014	0.020	0.084	0.077	0.054
μ_t (ksi)	5.1	8.6	17.8	11.2	9.7

Table 6. Tensile data for transverse/circumferential orientation: -T4 temper.

Alloy	6061 (F)	6061 (P)	2139 (P)	2050 (P)	2043 (B)
σ_{uts} (ksi)	35.8	37.8	63.1	62.8	54.5
σ_{ys} (ksi)	17.4	20.0	40.9	39.8	34.1
$\Delta\sigma_{form}$ (ksi)	18.4	17.7	22.3	23.0	20.4
e_u (%)	22.2	20.1	23.3	20.0	19.1
e_t (%)	32.5	29.4	32.4	24.0	22.4
AR (%)	43.7	44.6	44.0	28.6	23.6
K (ksi)	64.4	65.4	96.9	97.0	83.3
n	0.247	0.221	0.163	0.165	0.154
μ_r (ksi)	0.015	0.020	0.079	0.073	0.054
μ_t (ksi)	8.6	8.5	16.8	12.3	9.8

Table 7. Ranking of candidate alloys by selective metrics and differentiated by product form.

Rolled Plate

Alloy	Temper	Orient'n	AR	n	μ_r
AA 6061	-O	(L+T)/2	58.2	0.215	0.004
		Rank	1	4	6
	-T4	(L+T)/2	47.0	0.223	0.020
		Rank	2	3	3
AA 2139	-O	(L+T)/2	38.6	0.286	0.010
		Rank	4	1	5
	-T4	(L+T)/2	44.1	0.163	0.082
		Rank	3	6	1
AA 2050	-O	(L+T)/2	28.5	0.267	0.011
		Rank	5	2	4
	-T4	(L+T)/2	26.4	0.166	0.075
		Rank	6	5	2

AR ranking: AA 6061-O; AA 6061-T4; AA 2139-T4

n ranking: AA 2139-O; AA 2050-O; AA 6061-O

μ_r ranking: AA 2139-T4; AA 2050-T4; AA 2139-O

Roll Ring Forging

Alloy	Temper	Orient'n	AR	n	μ_r
AA 6061	-O	(A+C)/2	54.5	0.232	0.003
		Rank	1	3	6
	-T4	(A+C)/2	38.5	0.245	0.015
		Rank	2	2	2
AA 2219	-O	(A+C)/2	---	0.207	0.011
		Rank	---	4	4
AA 2050	-O	(A+C)/2	35.5	0.197	0.014
		Rank	3	5	3

Cast and Homogenized Billet

Alloy	Temper	Orient'n	AR	n	μ_r
AA 2043	-O	(A+C)/2	16.1	0.271	0.006
		Rank	5	1	5
	-T4	(A+C)/2	24.6	0.154	0.054
		Rank	4	6	1

AR ranking: AA 6061-O; AA 6061-T4; AA 2050-0

n ranking: AA 2043-O; AA 6061-T4; AA 6061-O

μ_r ranking: AA 2043-T4; AA 6061-T4; AA 2050-O

Table 8. Ranking of the top three candidate alloys/tempers/product forms for all formability metrics compared with benchmark AA 6061-O forging data.

Ranking	AR (%)	n (x 10^{-2})	μ_r (x 10^{-3} ksi)	r-ratio (L/A)	μ_t (ksi)
#1	**AA 2139-T4 (P)** *L= 44.2* *T= 44.0*	**AA 2139-O (P)** *L= 28.7* *T= 28.4*	**AA 2139-T4 (P)** *L= 84* *T= 79*	**AA 2043-O (B)** *max.= 0.85* *min.= 0.75*	**AA 2139-T4 (P)** *L= 17.8* *T= 16.8*
#2	**AA 2139-O (P)** *L= 37.6* *T= 39.6*	**AA 2043-O (B)** *A= 26.8* *C= 27.4*	**AA 2050-T4 (P)** *L= 77* *T= 73*	**AA 2043-T4 (B)** *max= 0.82* *min.= 0.71*	**AA 2050-T4 (P)** *L= 11.2* *T= 12.3*
#3	**AA 2050-O (F)** *A= 33.6* *C= 37.3*	**AA 2050-O (P)** *L= 26.3* *T= 27.7*	**AA 2043-T4 (B)** *A= 54* *C= 54*	**AA 2139-O (P)** *max= 0.78* *min.= 0.59*	**AA 2043-T4 (B)** *A= 9.7* *C= 9.8*
Benchmark	**AA 6061-O (F)** *A= 49.0* *C= 60.0*	**AA 6061-O (F)** *A= 23.8* *C= 22.6*	**AA 6061-O (F)** *A= 3* *C= 3*	**AA 6061-O (F)** *max= 0.65* *min.= 0.48*	**AA 6061-O (F)** *A= 3.4* *C= 1.1*